

PHYSICAL PROPERTIES OF YOUNG BROWN DWARFS AND VERY LOW-MASS STARS INFERRED FROM HIGH-RESOLUTION MODEL SPECTRA

EMILY L. RICE^{1,2}, T. BARMAN³, IAN S. MCLEAN¹, L. PRATO³, J. DAVY KIRKPATRICK⁴

Draft copy October 20, 2021

ABSTRACT

By comparing near-infrared spectra with atmospheric models, we infer the effective temperature, surface gravity, projected rotational velocity, and radial velocity for 21 very-low-mass stars and brown dwarfs. The unique sample consists of two sequences in spectral type from M6–M9, one of 5–10 Myr objects and one of >1 Gyr field objects. A third sequence is comprised of only \sim M6 objects with ages ranging from <1 Myr to >1 Gyr. Spectra were obtained in the *J* band at medium ($R\sim 2,000$) and high ($R\sim 20,000$) resolutions with NIRSPEC on the Keck II telescope. Synthetic spectra were generated from atmospheric structures calculated with the PHOENIX model atmosphere code. Using multi-dimensional least-squares fitting and Monte Carlo routines we determine the best-fit model parameters for each observed spectrum and note which spectral regions provide consistent results. We identify successes in the reproduction of observed features by atmospheric models, including pressure-broadened K I lines, and investigate deficiencies in the models, particularly missing FeH opacity, that will need to be addressed in order to extend our analysis to cooler objects. The precision that can be obtained for each parameter using medium- and high- resolution near-infrared spectra is estimated and the implications for future studies of very low mass stars and brown dwarfs are discussed.

Subject headings: infrared: stars — open clusters and associations: individual (Upper Scorpius, TW Hydrae Association) — stars: atmospheres — stars: low-mass, brown dwarfs — techniques: spectroscopic

1. INTRODUCTION

Determining the physical properties of brown dwarfs and very low-mass stars is important for our understanding of a broad range of topics including star and planet formation, circumstellar disks, dust formation in cool atmospheres, and the initial mass function. The direct measurement of mass and/or radius for a brown dwarf or very low-mass stars is possible only for certain binary systems, which are rare⁵. Determining other physical properties like effective temperature and surface gravity from bolometric luminosity estimates requires a precise distance measurement and assumptions about age (to determine effective temperature) plus mass and radius (to infer surface gravity from evolutionary models). Although radius is not expected to change very much for objects older than a few 100 Myr, reliance on evolutionary models is problematic as they are poorly calibrated at young ages. Commonly used conversions from spectral type to effective temperature (e.g. Golimowski et al. 2004 for field objects and Luhman et al. 2003 for young M dwarfs) rely on model isochrones and monotonic relationship between spectral type and effective temperature, which might not accurately represent the com-

plicated formation and evolution of very-low-mass objects (e.g. Stassun et al. 2006). Evolutionary models also require atmosphere models to provide boundary conditions. Thus, synthetic spectra from such atmosphere models potentially offer a more direct method of inferring physical properties by comparison with observed spectra.

The NIRSPEC Brown Dwarf Spectroscopic Survey (BDSS, McLean et al. 2003, 2007) is a large sample of high-quality near-infrared spectra obtained with the Keck II 10-meter telescope. One of the goals of the BDSS is to provide as direct a measurement of effective temperature, surface gravity, and metallicity as is possible for non-eclipsing objects. In principle this can be accomplished by comparing observed infrared spectra with synthetic spectra from atmosphere models, without relying on spectral type, distance measurements, or estimates of radius, mass, and age. Other authors have applied this promising but as yet imperfect technique to brown dwarfs. The primary difficulty of applying this method to low-mass stars and brown dwarfs is the complexity of the spectra to be modeled, leading to imposed limitations on resolution, wavelength range, and/or sample size. For example, Mohanty et al. (2004a,b) used narrow wavelength ranges at high resolution and Cushing et al. (2008) used a broad wavelength range at low resolution. Reiners et al. (2007) combined high-resolution spectra and broad wavelength coverage for a small sample of objects.

Many uncertainties remain in the determination of physical properties from the comparison of observed and synthetic spectra so it is important to establish the utility of this method using a larger sample of objects and a broader wavelength range. We accomplish this

¹ Department of Physics and Astronomy, UCLA, Los Angeles, CA 90095-1562

² Current address: American Museum of Natural History, Central Park West at 79th Street, New York, NY 10024-5192, erice@amnh.org

³ Lowell Observatory, 1400 West Mars Hill Road, Flagstaff, AZ 86001

⁴ Infrared Processing and Analysis Center, California Institute of Technology, Pasadena, CA 91125

⁵ An archive of very-low-mass binaries is maintained by N. Siegler (<http://vlbinaries.org/>); only a small fraction of these are double-lined spectroscopic binaries (DoS2,000) and high-resolution

($R \sim 20,000$) J -band spectra from the extensive BDSS data base⁶. Our goal is to show the extent to which synthetic spectra can be used to derive physical properties (effective temperature [T_{eff}], surface gravity [$\log(g)$], projected rotational velocity [$v \sin i$], and radial velocity [RV]) rather than the measurement and analysis of trends in the observational data. This paper focuses on field (≥ 1 Gyr) and young (1 to <100 Myr) M dwarfs, the majority of which are predicted to be substellar. Future papers will deal with a larger sample of young M dwarfs, young and field L dwarfs, and finally T dwarfs.

Section 2 describes the target selection, NIRSPEC observations, and data reduction. Section 3 outlines the calculation of atmospheric structures and synthetic spectra with the PHOENIX model atmosphere code and our novel spectral fitting method. Section 4 presents the analysis of the spectral fits, including an overview of the results for each resolution and wavelength range and for the inferred physical properties. Our results are discussed in § 5. Section 6 summarizes our conclusions and the implications of this work for future studies of brown dwarfs.

2. OBSERVATIONS AND DATA REDUCTION

2.1. Sample Selection

The sample of 21 objects constitutes three overlapping subsamples: 1) young (~ 5 – 10 Myr) objects with spectral types from M6 to M8.5, 2) field objects (≥ 1 Gyr) with spectral types from M5.5 to M9, and 3) \sim M6 objects with ages from $\lesssim 1$ Myr to ≥ 1 Gyr. Targets were selected based on published estimates of spectral type (M5.5 to M9), brightness ($J < 14.5$), and age. The names, spectral types, coordinates, and J -band magnitudes of the sample are listed in Table 1. Often the sample contains more than one object of a given spectral type and age to look for possible differences between objects (effects of multiplicity, rapid rotation, etc.) and to aid in identifying fiducial objects with well-determined physical properties. Ages of young objects are determined from membership in near-by star-forming regions and moving groups or confirmed companionship to known young stars age ~ 1 Myr to $\lesssim 100$ Myr, with the exception of 2MASS 0608–27, which has not been definitively associated with any other young objects. The young spectral type sequence contains objects with ages ~ 5 – 10 Myr in order to avoid the complications introduced by extinction, ongoing accretion, and veiling. The age sequence of \sim M6 objects necessarily contains younger objects that show signs of accretion activity and higher extinction. The majority of our targets have $A_V \sim 0$ with no evidence for ongoing accretion, although a few objects may retain cool disks. The majority of objects making up the 5– 10 Myr sequence are confirmed low-mass members of the Upper Scorpius OB association, with additional young brown dwarfs from the ~ 10 Myr-old TW Hydrae Association (e.g. Zuckerman & Song 2004; Barrado y Navascués 2006). The sample properties are summarized in Table 2.

2.2. Observations

Observations were made between 2000 December and 2009 April as part of the NIRSPEC Brown Dwarf Spectroscopic Survey (BDSS, McLean et al. 2003, 2007). NIRSPEC is the cryogenic cross-dispersed echelle spectrometer on the Keck II 10-m telescope on Mauna Kea, Hawaii (McLean et al. 1998, 2000). NIRSPEC has two modes, a cross-dispersed echelle mode and a non-echelle mode in which the echelle grating is replaced with a mirror and the cross-disperser provides the spectral dispersion. Both of these modes were employed with the NIRSPEC-3 (N3) filter, which approximates standard J -band coverage (1.143 – $1.375 \mu\text{m}$). In echelle mode eight usable dispersion orders (65 to 58) are captured on the detector. Because the spectral interval captured by the detector is slightly smaller than the free spectral range in each order, there are small gaps, increasing with wavelength, in the total spectral coverage. The exact wavelength ranges for each dispersion order are listed in the headings in Section 4.1. The slit width was two pixels ($0''.38$) for non-echelle observations and three pixels ($0''.432$) for echelle observations. The resolving power in J -band is approximately $R = \lambda / \Delta\lambda = 2,000$ (“medium” resolution) in non-echelle mode and $R = 20,000$ (“high” resolution) in echelle mode. Throughout the paper medium-resolution J -band spectra will be referred to by the filter name “N3” and high-resolution spectra by the number of the dispersion order.

Observing methods are described in detail in McLean et al. 2003 (medium resolution) and McLean et al. 2007 (high resolution); the following is a brief summary and explanation of departures from those methods. In both modes observations were made in pairs, nodding along the slit between each observation so that traces were separated by $20''$ on the $42''$ -long slit (medium resolution) and by $7''$ on the $12''$ -long slit (high resolution). For some recent high-resolution observations the size of the nod was reduced to avoid problems from an intermittent quadrant in the slit-viewing camera. During these occasions (2006 May and later) the nod size was at least $2''$ so that the dispersed traces would be well-separated on the slit. Integration time was 600 seconds per nod for all echelle mode observations except those on 2006 May 19 and 20, which were 300 seconds per nod. Medium-resolution observations were typically 300 seconds per nod. Total integration times per object are listed in Table 1. A0 V stars were observed at an airmass very close to that of the target object (typically <0.1 airmass difference) to calibrate for telluric absorption features. Arc lamp spectra were obtained at least once per night, and white-light spectra and corresponding dark frames were obtained for flat-fielding.

2.3. Data Reduction Methods

All of the observed data were reduced with the REDSPEC IDL-based software package⁷, described in McLean et al. (2003, 2007). The package performs standard bad pixel interpolation, dark subtraction, and flat-fielding as well as spatial rectification of curved spectra. Spectra are rectified and extracted in differenced nod pairs so that the sky background and OH emission lines are removed. Spectra were extracted by summing over

⁶ A public archive is maintained by I. S. McLean and collaborators (<http://www.astro.ucla.edu/~mclean/BDSSarchive/>)

⁷ <http://www2.keck.hawaii.edu/inst/nirspec/redspec.html>

7–15 pixels dependent on seeing then subtracted again to produce a positive spectrum with residual sky emission features removed. A0 V star spectra were reduced the same way, and target spectra were divided by the A0 V star spectrum to remove telluric features and multiplied with a $T_{eff} = 9500$ K blackbody spectrum to restore the true slope. At medium resolution Pa β absorption at $\lambda=1.2822 \mu\text{m}$ in the A0 V star spectrum is removed by interpolation, and at high resolution order 59 was not divided by an A0 V as it lacks strong telluric lines. Medium-resolution spectra were wavelength calibrated using Ne and Ar arc lamp lines, and high-resolution spectra with OH night sky lines, which were found to be highly stable and well-distributed across orders. Seven high-resolution dispersion orders (58–65, excepting 60) were reduced. Order 60 was not reduced because the OH night sky lines are blended with O₂ emission bands at 1.26–1.28 μm (Rousselot et al. 2000) making wavelength calibration and sky subtraction considerably more difficult. Each reduced spectrum was continuum normalized, and multiple nod pairs were averaged together to increase SNR. High-resolution spectra were shifted to the heliocentric reference frame.

Because the sample objects were selected in order to minimize the effects of extinction, only GY 5 required correction for its relatively large extinction, $A_V \sim 5$. The medium-resolution N3 spectrum was dereddened as described in McGovern (2005). High-resolution observations were not dereddened because the spectra cover such narrow wavelength ranges and are considered individually in the analysis, making differences in the pseudo-continuum level caused by reddening relatively unimportant.

3. MODEL ATMOSPHERES AND SYNTHETIC SPECTRA

3.1. The PHOENIX Code

The PHOENIX code was developed by Peter Hauschildt and collaborators beginning about 20 years ago, originally to model radiative transfer in supernova remnants. More recent versions of the code have been successfully applied to modeling stellar, substellar, and planetary atmospheres (Hauschildt et al. 1997, 1999; Allard et al. 2001; Barman et al. 2001). Some of the capabilities and features of PHOENIX are reviewed by Baron et al. (2003). Atmospheres are constructed by calculating temperature and pressure in each of 64 spherically-symmetric layers. The PHOENIX code determines radiative fluxes through the layers under the assumptions of hydrostatic equilibrium, radiative-convective equilibrium, and chemical equilibrium. The code begins with the results of a previously calculated structure, as an initial guess, and iterates toward the new solution by changing the radiative-convective temperatures at each layer via a modified Unsöld-Lucy temperature correction procedure (Hauschildt et al. 2003). Models were run for at least 20 iterations, which was sufficient in most cases to reach convergence. Convergence of a model is based on energy conservation and determined by an upper-limit on the percentage difference between the radiative-convective flux and the desired model flux (σT_{eff}^4), typically 5% or less at all layers. The output for converged atmospheres includes spectral energy distributions (SEDs) from 10 \AA to 1 mm with a resolution of 4 \AA through the

optical and near-infrared. From a converged atmospheric structure the PHOENIX code is used to produce a synthetic spectrum for a selected wavelength range (i.e., the J band) and numerical resolution, up to 500,000 wavelength elements in total.

3.2. Brown Dwarf Model Atmospheres

To match our observational sample we calculate model atmospheres for effective temperatures from 1800 K to 3000 K in intervals of 50 K and surface gravities from $\log(g) = 3.0$ to 6.0 in intervals of 0.1 dex. For this temperature range the *dusty* version of the PHOENIX model code is applicable. In this version, dust is formed in chemical equilibrium conditions and remains where it is formed in the atmosphere; the removal of dust by dynamical processes is ignored. At low temperatures where more dust is created ($T_{eff} \leq 2200$ K), the models often do not converge because of the drastic effects dust production has on the temperature structure. Instead, the temperature iterations will cause fluctuations around the converged solution. In these cases we manually chose the temperature-pressure structure with the smallest difference between calculated and prescribed flux (σT_{eff}), which was comparable to the differences for automatically converged models. All dust is created as pure, single-species, spherically-symmetric grains that follow an interstellar grain-size distribution (Allard et al. 2001). Model calculations incorporate some updates to the Allard et al. (2001) models, including solar abundances from Asplund et al. (2005), the FeH line list from Dulick et al. (2003), the CrH line list from Burrows et al. (2002), and the H₂O line list from Barber et al. (2006). The incorporation of the new FeH line list causes the most drastic change from previous generations of PHOENIX models and is discussed in detail in § 5.2. The differences are most evident in the medium- and high-resolution spectra and have little effect on the atmospheric structures. We integrate under the SEDs and compare the total flux to σT_{eff}^4 , and the differences were typically less than 2% but up to 5% for models with $T_{eff} < 2000$ K. Figure 1 shows the structures and SEDs for a range of effective temperatures at a surface gravity of $\log(g)=5.0$ and for a range of surface gravities at $T_{eff}=2600$ K. The non-smoothness in the structures at cool temperatures and low pressures are induced by dust formation and are mainly above the near-infrared photosphere, which lies at approximately 10^4 – 10^7 dynes cm^{-2} depending on effective temperature and surface gravity.

Pressure-broadening of strong lines impacts both the structure and the emergent spectrum of an atmosphere by adding opacity at wavelengths up to thousands of angstroms outside of the line center (e.g. Burrows et al. 2000; Allard et al. 2001). The numerical treatment of Van der Waals broadening in the PHOENIX models is described in Schweitzer et al. (1996). A more detailed treatment of the line broadening incorporates multiple perturbers in calculating the line wings (Allard et al. 2005). We tested this treatment and found that the differences in structures, SEDs, and high-resolution spectra were minimal for the temperatures and surface gravities under consideration. We also experimented with how widely the K and Na line profiles are calculated from

the line center. This is particularly important for alkali lines in the optical that have wings extending thousands of angstroms and contribute a large amount of opacity; when the line profiles are truncated it affects the atmospheric structure. The minimum width of the line profile above which there was not a noticeable difference was used. The consideration of line broadening will be more crucial for cooler atmosphere models (i.e. T dwarfs) for which dust opacity no longer dominates.

Medium-resolution synthetic spectra were calculated for the wavelength range 1.1–2.5 μm at 0.3 \AA resolution to oversample the instrumental resolution for the non-echelle (medium resolution, $R \sim 2,000$) mode of NIRSPEC at all near-infrared bands. For the current analysis only the *J*-band spectra are considered, but future papers will extend this study to *H*- and *K*-band BDSS data. High-resolution synthetic spectra were calculated at 0.03 \AA resolution for the wavelength range 1.1–1.4 μm to cover the entire *J* band and oversample the instrumental dispersion of NIRSPEC by a factor of 5–6 at those wavelengths (McLean et al. 2007, Table 2). The output of the PHOENIX code can be used to identify the most prevalent atomic, molecular, and dust grain opacity sources.

3.3. Spectral Fitting

The MPFIT IDL code developed by Markwardt (2009) was used to implement Levenberg-Marquardt least-squares minimization and determine the best-fit model parameters for each spectrum individually. The fit parameters are T_{eff} and $\log(g)$ from the grid of atmosphere models. Projected rotational velocity ($v \sin i$) is incorporated using standard Unsöld-type profile and convolution. Radial velocity (RV) is implemented as a shift in the observed spectrum onto the model wavelength array. A subroutine of the fitting code linearly interpolates between calculated models for each flux value in a given wavelength range in order to draw from an essentially smooth model grid. Once a new model is created for T_{eff} and $\log(g)$, the $v \sin i$ kernel and RV correction are applied. The $v \sin i$ kernel uses a limb-darkening coefficient of 0.6, which is typical although not well constrained. The flux values of synthetic spectra created using different limb-darkening coefficients differ by less than a tenth of one percent on average even at the lowest surface gravities and highest $v \sin i$ values considered.

The MPFIT routine was implemented two different ways. First, the initial T_{eff} and $\log(g)$ parameters were randomly drawn from the continuous range covered by linear interpolation of the calculated synthetic spectra. Some of the resulting best-fit parameters had much higher χ^2 values than was typical, indicating the code had found a local minimum rather than a global minimum, which is a known drawback of Levenberg-Marquardt least-squares minimization. The best-fit results were not sensitive to initial values of $v \sin i$ and RV. The best-fit parameters with lowest χ^2 values were averaged and set as the initial parameters for the second implementation of MPFIT. Following the Monte Carlo method, the initial guesses were kept constant and each flux point of the observed spectrum was randomly resampled from within the noise on that pixel. The distribution of the best-fit parameters then indicates the uncer-

tainty on the results from the noise in the data, which are adopted as our formal (relative) uncertainties, knowing that uncertainties in the model are much more difficult to characterize. Thus, like similar studies by Mohanty et al. (2004a), for example, our uncertainties represent relative precision and not accuracy. A veracious description of the uncertainties in the atmosphere models would require, for example, comparisons of results from different sets of models (e.g. Helling et al. 2008), which is beyond the scope of this paper. Typical results of this procedure are illustrated in Figure 2. All spectra were fit using 10^4 iterations of each implementation of MPFIT. Several spectra were fit with both 10^3 and 10^4 iterations, and the differences in resulting best-fit parameters were negligible.

The results for each spectral fit are presented in Tables 3–7. Tables 3 and 4 present the best-fit parameters for effective temperature and surface gravity, respectively, of each N3 spectrum and high-resolution dispersion order for the spectral type sequences. Each result is coded according to the quality for all orders based on visual inspection. No annotation corresponds to a good fit with minimal mismatches between the observed and synthetic spectra. Poorer fits are denoted by (*value*) for a few mismatches in depth or wing-shape for the strongest lines and by -(*value*)- for several mismatches. Entries that are struck are very poor fits that were not used in determining the adopted best-fit values. Note that the annotations are the same for both tables, even though it might be the case that the gravity is acceptable and the temperature is causing the poor fit, or vice versa. The quality of fits for each order are described in § 4.1 and for each parameter in § 4.2. Tables 5 and 6 present the best-fit parameters for the $\sim M6$ objects and are annotated the same way. The *adopted* T_{eff} and $\log(g)$ values are the mean of results from each dispersion order, weighted by the sum of the squared errors for all orders. With this method parameters that result in a good fit for one order but a poorer fit for other orders receive less weight. The velocity results presented in Table 7 are determined by the same weighted-mean method. The results are discussed by parameter in § 4.2.1–4.2.3. The N3-fit results were not used in the determination of the adopted best-fit values.

4. ANALYSIS

In the following sections we discuss the medium-resolution ($R \sim 2,000$, referred to as N3) and high-resolution ($R \sim 20,000$, referred to by dispersion order) synthetic and observed spectra in terms of major temperature- and gravity-dependent features. Then we summarize the fitting results for each parameter (T_{eff} , $\log(g)$, $v \sin i$, and RV).

4.1. Overview of Spectral Fits

N3 (1.143 – 1.375 μm) — The N3 filter on NIRSPEC corresponds to the *J* band, the wavelength regime in which flux of M dwarfs peaks. We use “N3” as shorthand for medium-resolution *J*-band spectra throughout the following sections. The morphology of observed spectra for M dwarfs with different spectral types and ages is shown in Figure 3. The overall shape of the N3 spectrum is sensitive to effective temperature, while the strengths of atomic lines are sensitive to surface gravity. At lower

temperatures the pseudo-continuum shape becomes more dependent on surface gravity. For most objects the N3 fits are very good, with the exception of the region between 1.20 and 1.24 μm , which is likely missing FeH opacity in the atmosphere models (see § 5.2), and at 1.28 μm where young and late-type objects might have weak Pa β emission. For some objects the depth of the H₂O band starting at 1.335 μm is not well matched, with the band being too strong in the atmosphere models for later-type objects. The apparent mismatch in the H₂O depth could also be a result of a poor fit to the pseudo-continuum level just before the H₂O band. Qualitatively the medium-resolution synthetic spectra provide good fits to the observed spectra, but the best-fit parameters are often discrepant from values predicted by the evolutionary models of Chabrier et al. (2000) and Baraffe et al. (2002).

Order 65 (1.16496 – 1.18207 μm) — The shortest-wavelength dispersion order features a strong K I doublet (resolved into a triplet at high resolution), a few weak Fe and Ti lines, and molecular lines of FeH and H₂O. The K I lines are sensitive to both temperature and surface gravity because both decreasing temperature and increasing surface gravity contribute to pressure-broadening (Figure 4). The strength of the molecular lines can break the degeneracy between high gravity and low temperature, particularly the strongest H₂O line at 1.16579 μm , which is weakly sensitive to gravity but strengthens greatly with decreasing temperature. The synthetic spectra reproduce the pressure-broadening of the K I lines for later spectral types (decreasing effective temperatures) and increasing age (increasing surface gravity) remarkably well. One difference between the order 65 observed and synthetic spectra is the shape of the pseudo-continuum between the K I lines at low temperatures. In the synthetic spectra the pseudo-continuum is more rounded as opposed to slightly flattened in the observed spectra. This is likely an indication that the alkali line profiles are not calculated as far into the wings as they should be. This was a known problem in the optical where the alkali lines are so strong that the calculation of the line profiles affects the atmospheric structure, but it is only a minor effect in the near-infrared.

The atmosphere models provide excellent fits to the order 65 observed spectra because of both the well-modeled K I lines and the lack of strong FeH lines in this particular wavelength region. Although even the strongest H₂O line is not strong enough to break the degeneracy between temperature and gravity with our fitting method, the linear relationship is so tight (see Figure 2, first panel) that constraining either temperature or gravity based on spectral type or evolutionary models, respectively, allows only a narrow range of values for the other parameter. In general the best-fit parameters from order 65 provide excellent fits to the other orders (with the notable exceptions of 62 and 63, see below), but in some cases the model fits produce K I lines that are too shallow in order 61 and Al I lines that are too deep with wings that are too broad in order 59. This may however be a consequence of the underrepresented FeH opacity in the atmosphere models that is changing the relative level of the pseudo-continuum and not a failure of the best-fit model parameters.

Order 64 (1.18293 – 1.20011 μm) — Order 64 con-

tains several atomic lines of Fe and Ti that are insensitive to temperature and gravity except at the low temperature/high gravity region of the parameter space covered in this analysis. This order provides less consistent fits for all but the earliest spectral type young objects because the FeH lines from the 0-1 band of F⁴ Δ -X⁴ Δ at 1.1939 μm that strengthens at lower temperatures and higher gravities are not reproduced by the atmosphere models (see § 5.2). Weaker atomic lines of Mg (1.1834 μm) and Ti (1.1896 & 1.1953 μm) identified in the model spectra are present in the observed spectra, although they are more blended with other features in the observed spectra than the atmosphere models predict (Figure 5). Order 64 produces good fits for the earliest spectral type young objects, with the fits becoming worse with later spectral types, resulting in high temperatures and low surface gravities that produce too-weak K I lines in order 65 and 61 and too-strong Al I lines in order 58.

Order 63 (1.20168 – 1.21938 μm) — The only atomic lines in order 63 are very weak so that the spectral features are primarily FeH and H₂O. As mentioned above, the FeH lines in the atmosphere models are too weak for all but the earliest spectral types of young objects. Figure 6 shows the general correspondence between absorption features and the increasing mismatch in their strengths at older ages and later spectral types. In both the models and the observations the strength of the FeH lines increases more dramatically with decreasing temperature and later spectral type than with decreasing gravity (the latter is more apparent at even lower temperatures than are shown in Figure 6). For young objects the correspondence between the locations of the lines, if not the strengths, is enough to provide a reasonable radial velocity measurement in most cases (see § 4.2.3).

Order 62 (1.22093 – 1.23899 μm) — Order 62 is also dominated by FeH lines that are not strong enough in the atmosphere models (Figure 7), particularly strong lines from the Q-branch of the F⁴ $\Delta_{7/2}$ -X⁴ $\Delta_{7/2}$ system from 1.221 to 1.223 μm and P- and R-branch lines throughout the order (McLean et al. 2007). Therefore order 62 is very similar to order 63 in terms of fitting observed spectra with synthetic spectra: for the most part the fit parameters are inconsistent except for radial velocity.

Order 61 (1.24081 – 1.25913 μm) — The longer-wavelength K I doublet in the J band falls in order 61 (Figure 8). While the atmosphere models again replicate the dependence of the K I lines on temperature and gravity very well, the weaker lines in this order are more problematic than in order 65 for two reasons. First, the model predicts evenly-spaced TiO lines that increase in strength with decreasing temperature, particularly at low gravity, but such features are not seen in the observations. This is likely because TiO lines in the observed spectra are blended with FeH lines that are too weak in the atmosphere models. Second, the lack of strong FeH in the models causes the wings of the K I lines and the pseudo-continuum shape to not match the observations. Therefore order 61 provides less consistent model fits than order 65 despite the strong, well-modeled K I lines.

Furthermore, the best-fit parameters do not fit other orders as well as the fits from order 65 that are also anchored by K I. For all but the earliest spectral types

(M6–M7), the best-fit parameters from order 61 result in Al I lines that are too strong in order 58 for the young objects and for the field objects, an unrealistic combination of high temperature and high gravity or low temperature and low gravity, both of which are manifested as poor fits in the other orders.

Order 59 (1.28262 – 1.30151 μ m) — The atomic lines in order 59 are weak, but they have interesting dependence on temperature and gravity. The strongest lines are Ti and Mn, with Fe and Cr lines being too weak to distinguish from noise on the observational spectra. The strongest Ti lines (1.2835 and 1.2850 μ m) and Mn line (1.2903 μ m) become broader and shallower with decreasing temperature at high gravity in the atmosphere models, but the trend is not as apparent in the observed spectra of field objects (Figure 9). At low gravity the lines do not change much with temperature. At high gravity and low temperature order 59 also contains FeH lines that are not strong enough in the models, rendering this order poor for model fits. The narrow lines from 1.297 to 1.301 μ m in the spectra of the young objects are weak telluric lines that were not removed because this order contains Pa β in the spectrum of an A0 V star. Order 59 provides consistent fits only for the earliest spectral type young objects.

Order 58 (1.30447 – 1.32370 μ m) — The longest-wavelength order contains an Al doublet that, in the atmosphere models, is sensitive to temperature at high gravities but nearly unchanged with temperature at $\log(g) \leq 4.0$ (Figure 10). The wings of the lines change shape with decreasing temperature as they become blended with strengthening molecular lines. This behavior is also seen in the high-gravity field objects, but not the young objects, for which the Al lines are stronger in the atmosphere models than in the observations. This is likely a consequence of the ubiquitous FeH absorption lowering the pseudo-continuum level making the Al lines appear relatively weaker than in the models, in which the FeH is too weak. Order 58 provides only slightly more consistent fits than order 59.

4.2. Spectral Fitting Results

4.2.1. Effective Temperature

Tables 3 and 5 present previously determined effective temperatures from the literature (column 3), the effective temperatures derived from model fits to medium-resolution N3 spectra (column 4) and each of seven dispersion orders of high-resolution spectra (columns 5–11), and our adopted best-fit temperatures (column 12). Previously published effective temperatures are a combination of measurements of bolometric luminosity (e.g. Vrba et al. 2004; Golimowski et al. 2004), spectral type to temperature conversions (Luhman et al. 2003; Mohanty & Basri 2003), and comparison with synthetic spectra at medium resolution (e.g. McGovern 2005). For many of the objects the range of temperatures reported in the literature is 300–400 K. Almost all of our adopted temperatures fall within or are very close to the range of previously determined temperatures; notable exceptions are TWA 5B and the field objects, discussed below. Adopted temperatures, which are from high-resolution fits, are also very similar to best-fit results from the N3 spectra, within ~ 60 K for objects earlier than M7 with

the exception of Gl 406, also discussed below. The results become less consistent for the later spectral type objects, with the spectral fits producing higher temperatures than predicted by spectral-type effective temperature relationships and bolometric measurements. For the most part the adopted temperatures decrease with later spectral types and are within ~ 100 K for objects of the same spectral type, again with the notable exception of TWA 5B. Both the N3 and echelle spectra of TWA 5B are lower signal-to-noise than average for our observations and the spectra are likely contaminated by light from the $J=7.67$ mag primary $\sim 2.5''$ away. Adopted effective temperatures for the field dwarf sequence also decrease for later spectral types, but they are even more dissimilar to previous temperature measurements.

The measured effective temperatures are most discrepant for the latest spectral type young objects, in particular TWA 5B, and the field (old, high gravity) objects Gl 406, LP 402-58, LP 412-31, and 2MASS 0140+27. For all of these objects the temperatures measured via spectral fitting are 200–350 K hotter than the effective temperatures determined by spectral type-effective temperature scales and bolometric luminosity measurements. The higher temperatures measured from spectral fitting are likely a consequence of the increasing importance of FeH absorption for cooler and higher gravity objects that is not reproduced by the atmosphere models (see § 5.2).

The age sequence of \sim M6 objects (Table 5) shows a very small spread in measured effective temperature. Interestingly the hottest temperature was measured for the unresolved binary Gl 577BC, which is the earliest spectral type object in the subsample. The average temperature for the objects is 2880 K, with a standard deviation of 60 K, which, although cooler than the temperature of 2990 K for a young M6 on the Luhman et al. (2003) scale, is promising for the development of a spectral type-effective temperature scale that is consistent for objects with a range of properties (e.g., age, rotation, and binarity) and calibrated by benchmark objects for which observed properties are successfully reproduced by atmosphere models.

Uncertainty resulting from noise in the observed spectra is determined via the standard deviation of the best-fit effective temperatures from flux-re-sampled spectra, which is typically $\lesssim 10$ K but as high as 30 K. Systematic uncertainty in the accuracy of the atmosphere models likely dominates the total uncertainty in the results, although as discussed above uncertainties in the models are difficult to quantify (see § 3.3). The standard deviations of best-fit effective temperatures from 10^4 iterations with varied initial parameters are typically 100–200 K. This is similar to the standard deviation of the best-fit effective temperatures from all orders, which is additionally subject to varying levels of fidelity between the observations and the models (described in § 4.1). The systematic uncertainties in effective temperature are much lower for the medium-resolution spectra, typically $\lesssim 50$ K. The implications of the relative uncertainties from high- and medium-resolution spectra are discussed in § 5.1.

4.2.2. Surface Gravity

The surface gravity measurements are presented in Tables 4 and 6. Previous studies have discovered gravity-sensitive features and spectral indices in the

near-infrared (e.g. Gorlova et al. 2003; McGovern et al. 2004; Allers et al. 2007) with low ($R \sim 300$) and medium ($R \sim 2,000$) spectra, notably a sharply peaked H -band spectrum (from increased H_2O absorption shortward of the peak in H -band flux) and weaker atomic lines (K I and Na I). Our analysis differs from previous work in that surface gravity and effective temperature are determined simultaneously and at higher resolution. For young objects, the adopted $\log(g)$ from high-resolution fits is within 0.3 dex of the best-fit results for the medium-resolution spectra, with the exception of the TW Hydrae members and 2MASS 0608–27. For these objects the medium-resolution fits produced surface gravities nearly an order of magnitude lower than expected for their temperatures and ages based on the evolutionary models of Chabrier et al. (2000) and Baraffe et al. (2002) (hereafter DUSTY00), an indication that high-resolution spectra are better for examining gravity-sensitive features than medium-resolution spectra. For field objects the medium-resolution fits produce gravities that are higher than physically reasonable according to the DUSTY00 evolutionary models. Such high gravities are likely a result of the N3 fits being affected by the missing FeH opacity in the atmosphere models. The surface gravity measurements for Upper Scorpius objects have a mean of 3.87, which is very close to the mean of $\log(g)=3.91$ for 5 Myr objects between 2500 and 3000 K predicted by the DUSTY00 evolutionary models. As shown in Figure 18, the distribution of measured surface gravities is only slightly wider than predicted by the DUSTY00 evolutionary models, with outlying values for USco 66AB ($\log(g)=4.26$) and DENIS 1619–24 ($\log(g)=3.49$). The relatively high $v \sin i$ of USco 66AB or higher-order unresolved binarity may contribute to the high surface gravity. Fits to spectra of DENIS 1619–24, on the other hand, result in a low surface gravity despite the high $v \sin i$ and possible binarity. There is no straightforward explanation for the outliers, but they are consistent with the DUSTY00 evolutionary models within the systematic uncertainty in $\log(g)$, ~ 0.5 dex (see below).

The surface gravity of field dwarfs as measured by fits to the high resolution spectra are somewhat higher than allowed by the DUSTY00 evolutionary tracks, but the measurements also have higher uncertainty because of the increasing mismatch between observed and model spectra for later spectral types and cooler temperatures, caused in large part by the atmosphere models lacking FeH opacity. The surface gravities measured from the N3 spectra are even higher, again suggesting that high-resolution spectra are required to accurately measure surface gravity. It should be noted, though, that our adopted gravities are the weighted mean of results from individual orders that are often either much lower or much higher than what is predicted by the DUSTY00 evolutionary models.

The age sequence of M6 objects (Table 6) generally shows the predicted trend of increasing surface gravity with age, although it is not strictly monotonic. The surface gravities are within ~ 0.2 dex of what is predicted by the isochrones for their age and effective temperature. A notable exception is 2MASS 2234+40AB, which has the highest effective temperature and surface gravity of the young (<100 Myr) objects. However, the adopted temperature and gravity are driven upwards by the poor fits

from orders 62 and 63, and temperature and gravity are degenerate such that lowering them both still produces a good spectral fit at high resolution.

Uncertainty resulting from noise in the observed spectra is determined via the standard deviation of the best-fit surface gravity from flux-re-sampled spectra, which is typically $\lesssim 0.1$ dex but as high as 0.16 dex. As with effective temperature, systematic uncertainty in the accuracy of the atmosphere models likely dominates the errors in the results. The standard deviation of best-fit surface gravities from the varied initial parameters and the standard deviation of the best-fit surface gravities from all orders were typically 0.4–0.6 dex. Systematic uncertainties in surface gravity from the medium-resolution spectra were on average ~ 0.4 dex. The implications of the relative uncertainties from high- and medium-resolution spectra are discussed in § 5.1.

4.2.3. Projected Rotational and Absolute Radial Velocities

Results for radial velocity and projected rotational velocity (RV and $v \sin i$) are presented in Table 7. We use the well-measured radial velocity of Gl 406 (19 ± 1 km s $^{-1}$) to establish systematic uncertainties in our measurements. The radial velocity of Gl 406 measured via spectral fitting is 18.7 km s $^{-1}$, which is consistent with the previously measured RV. Uncertainties are determined using the Monte Carlo implementation of MPFIT (see § 3.3) by taking the weighted mean of standard deviations of the re-sampled-flux results. Typical uncertainties are 1–2 km s $^{-1}$.

Radial and projected rotational velocities are measured for nine objects for the first time: five Upper Scorpius members, the Taurus object CFHT Tau 7, the young objects 2MASS 0608–27 and Gl 577BC, and the field dwarf LP 402-58. The average RV of the eight Upper Scorpius members in our sample is -7 km s $^{-1}$ with a dispersion of <2 km s $^{-1}$, consistent with the values of -5 km s $^{-1}$ and -6 km s $^{-1}$ determined by Muzerolle et al. (2003) and Kurosawa et al. (2006) for five and thirteen very-low-mass Upper Scorpius members, respectively. The measured radial velocity of SCH 1622–19 is furthest from the average of Upper Scorpius members, but still consistent with cluster membership considering our estimated uncertainty of 1–2 km s $^{-1}$. The measured radial velocity for CFHT Tau 7 is the peak of the histogram of Taurus members compiled by Bertout & Genova (2006), providing more evidence of Taurus membership for this recently-discovered object. RV results for TW Hydrae members are self-consistent with a mean of 8 km s $^{-1}$ and a standard deviation of <2 km s $^{-1}$; however, they are systematically lower than previous results by 1–6 km s $^{-1}$. The RV measurements from our analysis are consistent with other confirmed TW Hydrae members (e.g. Torres et al. 2003). The measured RV = -6.2 km s $^{-1}$ for Gl 577BC is very similar to the most recently measured RV of the primary, -6.5 km s $^{-1}$ (Nordström et al. 2004).

In order to test the results from the fitting procedure in which RV is one of four free parameters, we also measure RV by cross-correlating observed spectra with synthetic spectra calculated using the other best-fit parameters (T_{eff} , $\log(g)$, and $v \sin i$). The differences were typically less than 1 km s $^{-1}$ for individual orders, but up to several km s $^{-1}$ for order 63, particularly for field and

late-type objects. The average RV indicated the cross-correlation peak for each order was within 1–2 km s⁻¹ of the weighted mean RV from spectral fitting for all objects, indicating that precision is not sacrificed by including RV as a free parameter in the spectral fitting routine.

The derived $v\sin i$ values presented in Table 7 are either consistent with or higher than previously measured values. The high $v\sin i$ values for slow rotators are an unavoidable limitation of the instrumental resolution, which can be estimated using the known slowly-rotating standard Gl 406 ($v\sin i < 2.9$ km s⁻¹). Our measured $v\sin i$ of Gl 406 is 8 km s⁻¹, indicating the lower limit of measurable $v\sin i$ for the instrumental resolution. Two other objects have similar measured $v\sin i$ values (DENIS 1605–24 and SCH 1612–20); therefore, these are considered upper limits on their $v\sin i$. For the remaining objects the measured $v\sin i$ is similar to or slightly higher than $v\sin i$ values reported in the literature with the largest discrepancy for the field object LP 412-31. Both LP 412-31 and 2MASS 0140+27 are poorly reproduced by even the best-fit model parameters because of the lack of FeH opacity in the atmosphere models, which become a major source of spectral features for late M dwarfs. When the model spectrum does not match the observations well enough to constrain $v\sin i$, the fitting routine tends to return a high value of $v\sin i$ because it flattens out the model spectrum to compensate for mismatched features, thus minimizing the χ^2 . However, it is unclear why the best-fit for an object would produce a much higher $v\sin i$ when the previously published values are at or below the instrumental resolution, as is the case for LP 412-31. LP 412-31 is a strongly flaring M dwarf with very strong H α emission and magnetic field for its spectral type (Reid et al. 2002; Stelzer et al. 2006; Schmidt et al. 2007; Reiners & Basri 2007); perhaps the high $v\sin i$ measurement in the near-infrared is related to activity (the previously published $v\sin i$ was measured in the optical by Reid et al. 2002). The estimated precision of the $v\sin i$ measurements is ± 5 km s⁻¹ based on the typical standard deviation of measurements from each order.

5. DISCUSSION

5.1. Measuring the Physical Properties of Young Brown Dwarfs

Model fits to medium-resolution spectra produce consistent estimates of effective temperature but only weakly constrain surface gravity. On the other hand, high-resolution fits can be misleading because of the degeneracy between effective temperature, surface gravity, and $v\sin i$, which all contribute to broadening of the strongest atomic lines. Weaker molecular lines can help break this degeneracy, but the imperfect correspondence between observations and atmosphere models for the molecular lines, particularly FeH, confuse this issue. Therefore, the physical properties of brown dwarfs are likely best estimated by a combining both medium- and high-resolution for simultaneous fitting.

Representative observed and best-fit model spectra are presented in Figures 11–14. From a comparison of the best-fit spectra for the young (5 Myr) M6 object DENIS 1605–24 (Fig. 11) and the field (> 1 Gyr) M6 dwarf

Gl 406 (Fig. 12), it is evident that both the atomic and molecular lines are stronger in the field object than in the young object. The best-fit synthetic spectra are a better match for the young object than for the field object, particularly in the wings of the atomic lines. As described in § 3.2, this is possibly a result of the simplified line profiles that are currently implemented in the PHOENIX code. However, it is likely that shape of the line wings are also affected by blended molecular lines, especially FeH, that are not yet properly reproduced by the model (see § 5.2). It is promising, however, that in the spectra of DENIS 1605–24 there is a substantial correspondence between weak molecular lines in the model, especially evident in orders 63–61. The same lines are present in the best-fit spectra for Gl 406, but the line depths are far too shallow in the model even for this relatively hot object. Note that the missing molecular opacity in the model is also apparent in the medium-resolution spectrum of Gl 406 (last panel, gray) compared to the model spectrum with the weighted best-fit parameters from the high-resolution spectra. However, individual molecular lines can only be examined at high resolution.

Figures 13 and 14 are representative of the fits for later spectral type objects at different ages (~ 10 Myr: 2MASS 1139–31 and > 1 Gyr: LP 402-58). For 2MASS 1139–31 there are considerably more mismatches in the best-fit spectra than there are for the slightly younger and earlier-type object DENIS 1605–24. While the strong K I lines and many of the weaker features in the order 65 and 61 of 2MASS 1139–31 are reproduced, the strongest lines in orders 64, 59, and 58 are too deep in the model spectra. This can be attributed to the missing FeH opacity that dominates the molecular lines at these wavelengths: the pseudo-continuum level in the synthetic spectra is too high because of the missing opacity, resulting in atomic lines that are too deep when the synthetic pseudo-continuum is lowered to the observed pseudo-continuum. In the order 62 and 63 spectra the increasingly poor reproduction of the FeH bands at lower temperature and higher surface gravity is evident, although some features are coincident in wavelength. The best-fit parameters also reproduce the overall continuum shape of the medium-resolution spectrum of 2MASS 1139–31 (last panel of Fig. 13), although there is missing opacity from 1.19–1.24 μm , similar to Gl 406 in Fig. 12. The sharp drop in flux at 1.24 μm is less pronounced when a more detailed calculation of atomic line profiles are implemented in the code (see 3.2). The spectral fit for field M7 dwarf LP 402-58 (Fig. 14) also shows the success of the fit for the K I lines in order 65 and 61 and the too-deep Fe I, Mg I, and Al lines in order 64, 59, and 58. Similarly, the FeH bands in orders 63 and 62 are too weak in the model, likely contributing to the mismatches in atomic line depths at shorter wavelengths as well. The pseudo-continuum slope of the medium-resolution spectrum is flatter in the observed spectrum than in the model, suggesting that a cooler effective temperature provides a better fit. An effective temperature 100–200 K lower flattens out the pseudo-continuum but also produces a too-deep H₂O band at 1.34 μm and atomic lines that are too broad at high resolution, even in combination with lower surface gravity and $v\sin i$ values. Improving the FeH opacity in the atmosphere models is a likely first step to resolving this

issue.

Comparing our adopted values of T_{eff} and $\log(g)$ to isochrones of the DUSTY00 evolutionary models (Chabrier et al. 2000; Baraffe et al. 2002) provides a consistency check and a means of evaluating our results. Even though the DUSTY00 evolutionary models are poorly calibrated for the youngest objects, they can rule out unphysical values. For example, objects 5 Myr old with temperatures from 1800 K to 3000 K all have \log surface gravities between 3.81 and 3.96, objects older than 500 Myr in the same temperature range have \log surface gravities between 5.15 and 5.40, and no object of any age or effective temperature has a surface gravity over $\log(g)=5.40$.

All of our adopted temperatures and surface gravities are consistent with predictions of the DUSTY00 evolutionary models. Evolutionary tracks can be used to infer the masses and ages of objects from their measured temperatures and surface gravities. Adopted T_{eff} and $\log(g)$ values for the 5–10 Myr subsample (including 2MASS 0608–27) and additional objects with ages ≤ 1 –3 Myr are compared to the DUSTY00 tracks in Figure 18. Within the error bars all of the objects are consistent with the properties predicted for young (age < 20 Myr) brown dwarfs (mass $< 72 M_J$). Two slightly anomalous objects are DENIS 1619–24 (too low gravity) and USco 66AB (too high gravity), which are discussed above. All of the objects are well above the deuterium-burning mass limit ($\sim 13 M_J$, Chabrier et al. 2000).

The relative systematic uncertainties on the best-fit effective temperatures and surface gravities from high- and medium-resolution spectra indicate a promising method of inferring the physical properties of young brown dwarfs. Medium-resolution J -band spectra strongly constrain effective temperature of mid-late M dwarfs, but not surface gravity. Neither can medium-resolution spectra be used to measure $v \sin i$, which may influence surface gravity measurements. High-resolution spectra, particularly of the shorter-wavelength K I doublet in NIRSPEC dispersion order 65, strongly constrain surface gravity relative to effective temperature. Therefore, we anticipate that using a measurement of effective temperature from medium-resolution spectra to constrain the effective temperature for high-resolution spectral fitting will increase the accuracy of properties derived using high-resolution spectra. The measured range of $v \sin i$ values does not correlate with age or known binarity. Improvements in the model atmospheres that more consistently reproduce the spectral features of both young and field brown dwarfs will improve the accuracy of $v \sin i$ measurements and provide insight into the dependence of angular momentum evolution on mass and age.

5.2. FeH Oscillator Strengths

One of the glaring mismatches between observed and synthetic spectra is the apparently missing opacity from FeH bands, particularly in orders 62 and 63. Our model atmosphere calculations incorporate new FeH line list from Dulick et al. (2003) as an update to the previously used Phillips et al. (1987) line list. However, one key difference between the use of these line lists in the PHOENIX code is that oscillator strength scalings available for the Phillips et al. (1987) line list are not applied to the Dulick et al. (2003) line list. Burgasser et al.

(2003) shows that the *absorption coefficients* in the Dulick et al. (2003) line list correspond to absorption features in the medium-resolution J -band spectrum of a late-L dwarf (their Figure 2b). Our results indicate that the Dulick et al. (2003) line list, as incorporated into the PHOENIX code, fails to reproduce observed FeH absorption features.

Figures 15 and 16 illustrate the effects of different FeH line lists and oscillator strength scalings on synthetic spectra. Figure 15 shows J -band spectra synthetic spectra ($T_{eff}=2600$ K, $\log(g)=5.0$, convolved to match a medium-resolution NIRSPEC spectrum) for the Dulick et al. (2003) FeH line list, the Phillips et al. (1987) line list, and the “scaled” Phillips et al. (1987) line list, for which red-optical and near-infrared FeH band strengths are multiplied by factors of 10–20 (and for one band, 150). It is evident from comparison with the observed spectrum of 2MASS 0140+17 (M9) that the scaled FeH strengths using the Phillips et al. (1987) line lists match the observed spectra better, particularly the broad absorption features at 1.20 and 1.21 μm that are essentially absent in spectra with unscaled line lists. At this resolution the difference between the unscaled line lists is imperceptible, but the high-resolution spectra provide further insight. In Figure 16 the same synthetic spectra are convolved to match NIRSPEC dispersion order 63, and it is apparent that even the scaled Phillips et al. (1987) line list falls short of reproducing the observed spectrum of the M9 dwarf 2MASS 0140+27. The Dulick et al. (2003) list provides more individual lines in this wavelength range, but the lines are still far too weak. In a future paper we will quantify the shortcomings in the current FeH data by implementing scaling of the Dulick et al. (2003) line list in the PHOENIX code.

FeH is an important source of spectral features from the z band through the H band, particularly in the longer wavelength half of the J band (McLean et al. 2003; Cushing et al. 2003, 2005; McLean et al. 2007), and the features strengthen with decreasing effective temperature until $\sim L5$ (Kirkpatrick et al. 1999), when FeH begins to weaken through the L-T transition then strengthen in mid-to-late T dwarfs, possibly as cloud-clearing allows flux to escape from lower in the atmosphere where FeH remains as a gas (Burgasser et al. 2002; McLean et al. 2003; Cushing et al. 2008). Therefore, further study of FeH in the atmosphere models is necessary to extend our near-infrared spectral fitting analysis to L and T dwarfs as well as to shorter and longer wavelength observations.

Magnetic fields may also affect FeH strengths, and the Wing-Ford band of FeH ($\sim 1 \mu\text{m}$) has been used to measure magnetic field strengths in M dwarfs. However, strong magnetic fields actually weaken the magnetically-sensitive lines (see Reiners & Basri 2007, Figures 2–10). Therefore, if magnetic fields need to be included in the atmosphere models in order to reproduce observed FeH bands, it is likely a second-order effect to the overall scaling of the oscillator strengths.

5.3. Effects of Binarity

Unresolved binaries in the sample are Gl 577BC, USco 66AB, 2MASS 2234+40AB, and 2MASS 1207–39Ab. These binaries vary in mass ratio (q) from $q \sim 1$ (Gl 577BC: Lowrance et al. 2005, USco 66AB: Kraus et al. 2005, 2MASS 2234+40AB:

Allers et al. 2009) to $q \sim 0.3$ (2MASS 1207–39Ab; Mohanty et al. 2007). Additionally, DENIS 1619–24 is a candidate spectroscopic binary (Mohanty et al. 2005), and Slesnick et al. (2006) suggests that SCH 1622–19 might be an unresolved binary (a $\lesssim 175$ AU) based on overluminosity for its spectral type relative to other Upper Scorpius members on an H-R diagram. For our purposes the effects of unresolved binarity are minimal as long as the mass ratio is either very high or very low. The main concern is the effect of unresolved binarity on the estimate of $v \sin i$. Previous authors have noted that broadened absorption lines may be indicative of an unresolved binary (e.g. Simon et al. 2006). As shown in Figure 17, the velocity shift between components of a close binary can mimic a higher value of $v \sin i$. However, the RV-shift needed to reproduce the spectrum of USco 66AB ($v \sin i = 28 \text{ km s}^{-1}$), using the DENIS 1605–24 ($v \sin i \leq 7 \text{ km s}^{-1}$) as a template, is at least several times larger than the maximum possible velocity difference of the known binary. Two possibly unresolved binaries, DENIS 1619–24 and SCH 1622–19, are among the highest $v \sin i$ measurements, but they are not anomalous compared to other, apparently single, rapidly rotating objects. A future paper will explore this issue further by comparing spectral fitting results from spatially resolved (using NIRSPEC and Laser Guide Star Adaptive Optics, e.g. Konopacky et al. in prep.) and unresolved spectra of very low mass binaries.

6. CONCLUSIONS

We have estimated the effective temperature, surface gravity, absolute radial velocity and projected rotational velocity for a sample of young brown dwarfs and field M dwarfs. Comparison of high-resolution synthetic and observed spectra of young objects provide more accurate determination of surface gravity than from lower resolution observations. However, the small wavelength range and lack of fidelity of FeH line strength in the atmosphere models result in anomalously high temperatures for late-M type objects. Despite the mismatch in line strengths, radial velocity is well-determined for all but the coolest field objects considered in this analysis. Additionally, the richness of lines at high resolution breaks the degeneracy between sources of line-broadening so that $v \sin i$ is also well-determined for most objects. The principal results of the paper are as follows:

(1) Adopted (weighted-mean) effective temperatures from high-resolution spectral fits for objects M7 and earlier fall within or very close to previously published estimates and results from medium-resolution spectral fits. For objects M8 and later, temperatures from medium-resolution fits are similar to previously published values and temperatures from high-resolution fits are systematically too hot.

(2) Adopted (weighted-mean) surface gravities from high-resolution fits neatly separate objects with T_{eff} from 1800–3000 K according to age, with 1–10 Myr objects lying broadly between $\log(g)=3.5$ and 4.3, while objects from 0.5–5 Gyr are in the $\log(g)=5.2$ –5.4 range. Surface gravities from medium-resolution fits are generally similar to the adopted values except for M8–M9 young objects, which are systematically low, and field objects, which are systematically high.

(3) The age sequence of M6 objects yields an average

temperature of 2880 ± 60 K.

(4) For the Upper Scorpius objects the mean surface gravity is $\log(g)=3.87$, which is very close to the value of $\log(g)=3.91$ predicted by the DUSTY00 evolutionary model for 5 Myr objects between 2500 and 3000 K.

(5) FeH features are not yet properly reproduced by atmosphere models, and this impacts fitting spectra to high-resolution observations. The recent Dulick et al. (2003) line lists provide better correspondence for individual features, but the lines are not strong enough in the models. Improving FeH in the atmosphere models is urgently needed.

(6) Physical properties of brown dwarfs are likely best measured by comparing observed and synthetic spectra using a combination of medium- and high-resolution spectra simultaneously.

This work represents the first in a series of analysis of medium- and high-resolution observed and synthetic spectra of brown dwarfs. Future work will extend the study to later spectral types, cooler atmosphere models (where T_{eff} and $\log(g)$ might become more intertwined, e.g. Burgasser et al. 2006), and different dust treatments (i.e. the PHOENIX-*cond* models). Further analysis will also explore effects of metallicity on atmospheric structure and resultant spectra. While the focus thus far is on the large database of high-resolution spectra provided by the BDSS, some combination of high resolution and broad spectral coverage will likely prove ideal for accurately inferring the physical properties of brown dwarfs using atmosphere models. Therefore, we are developing a procedure to combine all available observed spectral data for simultaneous model fits.

The authors wish to thank the staff of the Keck Observatory for their outstanding support, including Joel Aycock, Randy Campbell, Al Conrad, Grant Hill, Jim Lyke, Steven Magee, Julie Renaud-Kim, Barbara Schaefer, Chuck Sorenson, Terry Stickel, and Cynthia Wilburn. Observing assistance from Antonia Hubbard, Quinn M. Konopacky, Gregory Mace, and Erin C. Smith and data reduction by Chalence Safranek-Schrader was greatly appreciated. E.L.R. acknowledges the hospitality of the research and administrative staff at Lowell Observatory. T.B. acknowledges the NASA Origins of Solar System program and the Mount Cuba Astronomical Fund for their generous support. I.S.M. acknowledges the staff of the UCLA Infrared Laboratory and colleagues James Graham (UCB), James Larkin (UCLA) and Eric Becklin (UCLA) for their support throughout the development of the NIRSPEC instrument. This paper benefited greatly from the detailed and thoughtful comments of the anonymous referee.

This research has made use of the NASA/IPAC Infrared Science Archive, which is operated by the Jet Propulsion Laboratory, California Institute of Technology, under contract with the National Aeronautics and Space Administration. This publication makes use of data from the Two Micron All Sky Survey, which is a joint project of the University of Massachusetts and the Infrared Processing and Analysis Center, funded by the National Aeronautics and Space Administration and the National Science Foundation. This research has benefited from the M, L, and T dwarf compendium housed

at DwarfArchives.org and maintained by Chris Gelino, Davy Kirkpatrick, and Adam Burgasser. This research has made use of the SIMBAD database, operated at CDS, Strasbourg, France and NASA's Astrophysics Data

System. Finally, the authors wish to extend special thanks to those of Hawaiian ancestry on whose sacred mountain we are privileged to be guests.

Facilities: Keck:II (NIRSPEC)

REFERENCES

- Allard, F., Hauschildt, P. H., Alexander, D. R., Tamanai, A., & Schweitzer, A. 2001, *ApJ*, 556, 357
- Allard, N. F., Allard, F., & Kielkopf, J. F. 2005, *A&A*, 440, 1195
- Allers, K. N., Jaffe, D. T., Luhman, K. L., Liu, M. C., Wilson, J. C., Skrutskie, M. F., Nelson, M., Peterson, D. E., Smith, J. D., & Cushing, M. C. 2007, *ApJ*, 657, 511
- Allers, K. N., Liu, M. C., Shkolnik, E., Cushing, M. C., Dupuy, T. J., Mathews, G. S., Reid, I. N., Cruz, K. L., & Vacca, W. D. 2009, *ArXiv e-prints*
- Ardila, D., Martín, E., & Basri, G. 2000, *AJ*, 120, 479
- Asplund, M., Grevesse, N., & Sauval, A. J. 2005, in *Astronomical Society of the Pacific Conference Series*, Vol. 336, *Cosmic Abundances as Records of Stellar Evolution and Nucleosynthesis*, ed. T. G. Barnes, III & F. N. Bash, 25–+
- Baraffe, I., Chabrier, G., Allard, F., & Hauschildt, P. H. 2002, *A&A*, 382, 563
- Barber, R. J., Tennyson, J., Harris, G. J., & Tolchenov, R. N. 2006, *MNRAS*, 368, 1087
- Barman, T. S., Hauschildt, P. H., & Allard, F. 2001, *ApJ*, 556, 885
- Baron, E., Hauschildt, P. H., Allard, F., Lentz, E. J., Aufdenberg, J., Schweitzer, A., & Barman, T. 2003, in *IAU Symposium*, Vol. 210, *Modelling of Stellar Atmospheres*, ed. N. Piskunov, W. W. Weiss, & D. F. Gray, 19–+
- Barrado y Navascués, D. 2006, *A&A*, 459, 511
- Basri, G., Mohanty, S., Allard, F., Hauschildt, P. H., Delfosse, X., Martín, E. L., Forveille, T., & Goldman, B. 2000, *ApJ*, 538, 363
- Béjar, V. J. S., Zapatero Osorio, M. R., & Rebolo, R. 1999, *ApJ*, 521, 671
- Bertout, C. & Genova, F. 2006, *A&A*, 460, 499
- Burgasser, A. J., Burrows, A., & Kirkpatrick, J. D. 2006, *ApJ*, 639, 1095
- Burgasser, A. J., Kirkpatrick, J. D., Burrows, A., Liebert, J., Reid, I. N., Gizis, J. E., McGovern, M. R., Prato, L., & McLean, I. S. 2003, *ApJ*, 592, 1186
- Burgasser, A. J., Marley, M. S., Ackerman, A. S., Saumon, D., Lodders, K., Dahn, C. C., Harris, H. C., & Kirkpatrick, J. D. 2002, *ApJ*, 571, L151
- Burrows, A., Marley, M. S., & Sharp, C. M. 2000, *ApJ*, 531, 438
- Burrows, A., Ram, R. S., Bernath, P., Sharp, C. M., & Milsom, J. A. 2002, *ApJ*, 577, 986
- Caballero, J. A. 2007, *A&A*, 466, 917
- Chabrier, G., Baraffe, I., Allard, F., & Hauschildt, P. 2000, *ApJ*, 542, 464
- Cushing, M. C., Marley, M. S., Saumon, D., Kelly, B. C., Vacca, W. D., Rayner, J. T., Freedman, R. S., Lodders, K., & Roellig, T. L. 2008, *ApJ*, 678, 1372
- Cushing, M. C., Rayner, J. T., Davis, S. P., & Vacca, W. D. 2003, *ApJ*, 582, 1066
- Cushing, M. C., Rayner, J. T., & Vacca, W. D. 2005, *ApJ*, 623, 1115
- Dahn, C. C., Harris, H. C., Vrba, F. J., Guetter, H. H., Canzian, B., Henden, A. A., Levine, S. E., Luginbuhl, C. B., Monet, A. K. B., Monet, D. G., Pier, J. R., Stone, R. C., Walker, R. L., Burgasser, A. J., Gizis, J. E., Kirkpatrick, J. D., Liebert, J., & Reid, I. N. 2002, *AJ*, 124, 1170
- Dulick, M., Bauschlicher, Jr., C. W., Burrows, A., Sharp, C. M., Ram, R. S., & Bernath, P. 2003, *ApJ*, 594, 651
- Gatti, T., Testi, L., Natta, A., Randich, S., & Muzerolle, J. 2006, *A&A*, 460, 547
- Gizis, J. E. 2002, *ApJ*, 575, 484
- Gizis, J. E., Monet, D. G., Reid, I. N., Kirkpatrick, J. D., Liebert, J., & Williams, R. J. 2000, *AJ*, 120, 1085
- Golimowski, D. A., Leggett, S. K., Marley, M. S., Fan, X., Geballe, T. R., Knapp, G. R., Vrba, F. J., Henden, A. A., Luginbuhl, C. B., Guetter, H. H., Munn, J. A., Canzian, B., Zheng, W., Tsvetanov, Z. I., Chiu, K., Glazebrook, K., Hovestren, E. A., Schneider, D. P., & Brinkmann, J. 2004, *The Astronomical Journal*, 127, 3516
- Gorlova, N. I., Meyer, M. R., Rieke, G. H., & Liebert, J. 2003, *ApJ*, 593, 1074
- Guieu, S., Dougados, C., Monin, J.-L., Magnier, E., & Martín, E. L. 2006, *A&A*, 446, 485
- Hauschildt, P. H., Allard, F., & Baron, E. 1999, *ApJ*, 512, 377
- Hauschildt, P. H., Barman, T. S., Baron, E., & Allard, F. 2003, in *Astronomical Society of the Pacific Conference Series*, Vol. 288, *Stellar Atmosphere Modeling*, ed. I. Hubeny, D. Mihalas, & K. Werner, 227–+
- Hauschildt, P. H., Baron, E., & Allard, F. 1997, *ApJ*, 483, 390
- Helling, C., Ackerman, A., Allard, F., Dehn, M., Hauschild, P., Homeier, D., Lodders, K., Marley, M., Rietmeijer, F., Tsuji, T., & Woitke, P. 2008, *ArXiv e-prints*, 809
- Kenyon, M. J., Jeffries, R. D., Naylor, T., Oliveira, J. M., & Maxted, P. F. L. 2005, *MNRAS*, 356, 89
- Kirkpatrick, J. D. 2008, in *Astronomical Society of the Pacific Conference Series*, Vol. 384, *14th Cambridge Workshop on Cool Stars, Stellar Systems, and the Sun*, ed. G. van Belle, 85–+
- Kirkpatrick, J. D., Reid, I. N., Liebert, J., Cutri, R. M., Nelson, B., Beichman, C. A., Dahn, C. C., Monet, D. G., Gizis, J. E., & Skrutskie, M. F. 1999, *ApJ*, 519, 802
- Kraus, A. L., White, R. J., & Hillenbrand, L. A. 2005, *ApJ*, 633, 452
- Kurosawa, R., Harries, T. J., & Littlefair, S. P. 2006, *MNRAS*, 372, 1879
- Lowrance, P. J., Becklin, E. E., Schneider, G., Kirkpatrick, J. D., Weinberger, A. J., Zuckerman, B., Dumas, C., Beuzit, J.-L., Plait, P., Malumuth, E., Heap, S., Terrile, R. J., & Hines, D. C. 2005, *AJ*, 130, 1845
- Lowrance, P. J., McCarthy, C., Becklin, E. E., Zuckerman, B., Schneider, G., Webb, R. A., Hines, D. C., Kirkpatrick, J. D., Koerner, D. W., Low, F., Meier, R., Rieke, M., Smith, B. A., Terrile, R. J., & Thompson, R. I. 1999, *ApJ*, 512, L69
- Luhman, K. L. 2006, *ApJ*, 645, 676
- Luhman, K. L. & Rieke, G. H. 1999, *ApJ*, 525, 440
- Luhman, K. L., Stauffer, J. R., Muench, A. A., Rieke, G. H., Lada, E. A., Bouvier, J., & Lada, C. J. 2003, *ApJ*, 593, 1093
- Markwardt, C. B. 2009, *ArXiv e-prints*
- Martín, E. L., Delfosse, X., & Guieu, S. 2004, *AJ*, 127, 449
- McGovern, M. R. 2005, PhD thesis, University of California, Los Angeles, United States – California
- McGovern, M. R., Kirkpatrick, J. D., McLean, I. S., Burgasser, A. J., Prato, L., & Lowrance, P. J. 2004, *ApJ*, 600, 1020
- McLean, I. S., Becklin, E. E., Bendiksen, O., Brims, G., Canfield, J., Figer, D. F., Graham, J. R., Hare, J., Lacayanga, F., Larkin, J. E., Larson, S. B., Levenson, N., Magnone, N., Teplitz, H., & Wong, W. 1998, in *Society of Photo-Optical Instrumentation Engineers (SPIE) Conference Series*, Vol. 3354, *Society of Photo-Optical Instrumentation Engineers (SPIE) Conference Series*, ed. A. M. Fowler, 566–578
- McLean, I. S., Graham, J. R., Becklin, E. E., Figer, D. F., Larkin, J. E., Levenson, N. A., & Teplitz, H. I. 2000, in *Society of Photo-Optical Instrumentation Engineers (SPIE) Conference Series*, Vol. 4008, *Society of Photo-Optical Instrumentation Engineers (SPIE) Conference Series*, ed. M. Iye & A. F. Moorwood, 1048–1055
- McLean, I. S., McGovern, M. R., Burgasser, A. J., Kirkpatrick, J. D., Prato, L., & Kim, S. S. 2003, *ApJ*, 596, 561
- McLean, I. S., Prato, L., McGovern, M. R., Burgasser, A. J., Kirkpatrick, J. D., Rice, E. L., & Kim, S. S. 2007, *ApJ*, 658, 1217
- Mohanty, S. & Basri, G. 2003, *ApJ*, 583, 451
- Mohanty, S., Basri, G., Jayawardhana, R., Allard, F., Hauschildt, P., & Ardila, D. 2004a, *ApJ*, 609, 854
- Mohanty, S., Jayawardhana, R., & Barrado y Navascués, D. 2003, *ApJ*, 593, L109
- Mohanty, S., Jayawardhana, R., & Basri, G. 2004b, *ApJ*, 609, 885
- . 2005, *ApJ*, 626, 498

- Mohanty, S., Jayawardhana, R., Huélamo, N., & Mamajek, E. 2007, *ApJ*, 657, 1064
- Muzerolle, J., Hillenbrand, L., Calvet, N., Briceño, C., & Hartmann, L. 2003, *ApJ*, 592, 266
- Nordström, B., Mayor, M., Andersen, J., Holmberg, J., Pont, F., Jørgensen, B. R., Olsen, E. H., Udry, S., & Mowlavi, N. 2004, *A&A*, 418, 989
- Phillips, J. G., Davis, S. P., Lindgren, B., & Balfour, W. J. 1987, *ApJS*, 65, 721
- Preibisch, T., Brown, A. G. A., Bridges, T., Guenther, E., & Zinnecker, H. 2002, *AJ*, 124, 404
- Reid, I. N., Kirkpatrick, J. D., Liebert, J., Gizis, J. E., Dahn, C. C., & Monet, D. G. 2002, *AJ*, 124, 519
- Reid, N. 2003, *MNRAS*, 342, 837
- Reiners, A. & Basri, G. 2007, *ApJ*, 656, 1121
- Reiners, A., Homeier, D., Hauschildt, P. H., & Allard, F. 2007, *A&A*, 473, 245
- Rousselot, P., Lidman, C., Cuby, J.-G., Moreels, G., & Monnet, G. 2000, *A&A*, 354, 1134
- Schmidt, S. J., Cruz, K. L., Bongiorno, B. J., Liebert, J., & Reid, I. N. 2007, *AJ*, 133, 2258
- Scholz, A., Jayawardhana, R., Wood, K., Meeus, G., Stelzer, B., Walker, C., & O'Sullivan, M. 2007, *ApJ*, 660, 1517
- Schweitzer, A., Hauschildt, P. H., Allard, F., & Basri, G. 1996, *MNRAS*, 283, 821
- Simon, M., Bender, C., & Prato, L. 2006, *ApJ*, 644, 1183
- Slesnick, C. L., Carpenter, J. M., & Hillenbrand, L. A. 2006, *AJ*, 131, 3016
- Slesnick, C. L., Hillenbrand, L. A., & Carpenter, J. M. 2008, *ApJ*, 688, 377
- Stassun, K. G., Mathieu, R. D., & Valenti, J. A. 2006, *Nature*, 440, 311
- Stelzer, B., Schmitt, J. H. M. M., Micela, G., & Liefke, C. 2006, *A&A*, 460, L35
- Teixeira, R., Ducourant, C., Chauvin, G., Krone-Martins, A., Song, I., & Zuckerman, B. 2008, *A&A*, 489, 825
- Tinney, C. G. & Reid, I. N. 1998, *MNRAS*, 301, 1031
- Torres, G., Guenther, E. W., Marschall, L. A., Neuhäuser, R., Latham, D. W., & Stefanik, R. P. 2003, *AJ*, 125, 825
- Vrba, F. J., Henden, A. A., Luginbuhl, C. B., Guetter, H. H., Munn, J. A., Canzian, B., Burgasser, A. J., Kirkpatrick, J. D., Fan, X., Geballe, T. R., Golimowski, D. A., Knapp, G. R., Leggett, S. K., Schneider, D. P., & Brinkmann, J. 2004, *AJ*, 127, 2948
- Wilking, B. A., Greene, T. P., & Meyer, M. R. 1999, *AJ*, 117, 469
- Wilking, B. A., Meyer, M. R., Robinson, J. G., & Greene, T. P. 2005, *AJ*, 130, 1733
- Zuckerman, B. & Song, I. 2004, *ARA&A*, 42, 685

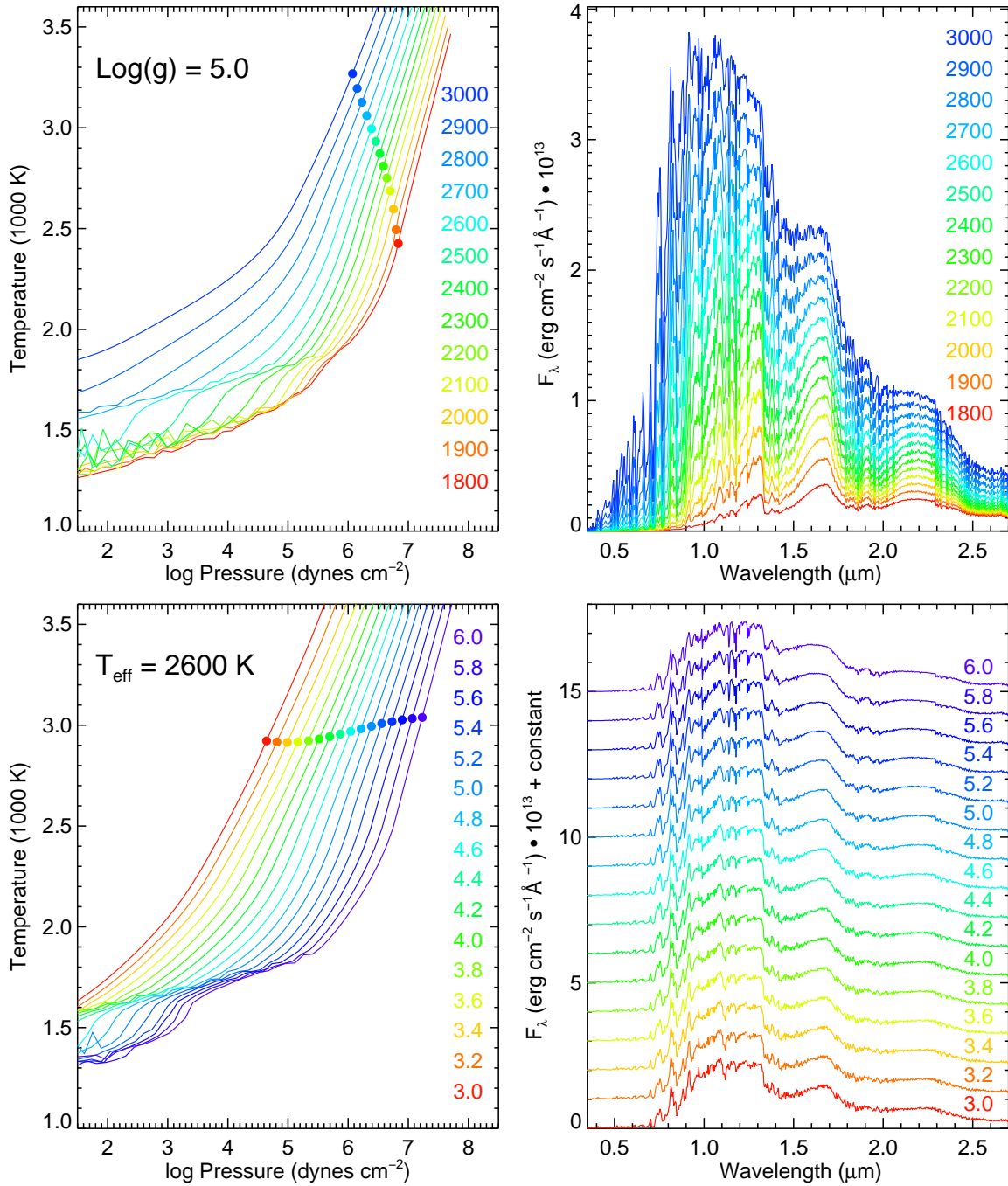


FIG. 1.— Left: Temperature-pressure profile of model atmosphere structures calculated using the PHOENIX code. Filled circles mark the near-infrared photosphere ($\tau_{\lambda=1.2 \mu\text{m}} = \frac{2}{3}$). Right: Spectral energy distribution (SED) for the same model atmospheres. The top plots display structures and SEDs calculated at $\log(g)=5.0$ for the entire range of effective temperatures. The bottom plots display structures and SEDs (offset by a constant) calculated at $T_{\text{eff}}=2600 \text{ K}$ for the entire range of surface gravities. Only half of the calculated structures and SEDs are shown for clarity.

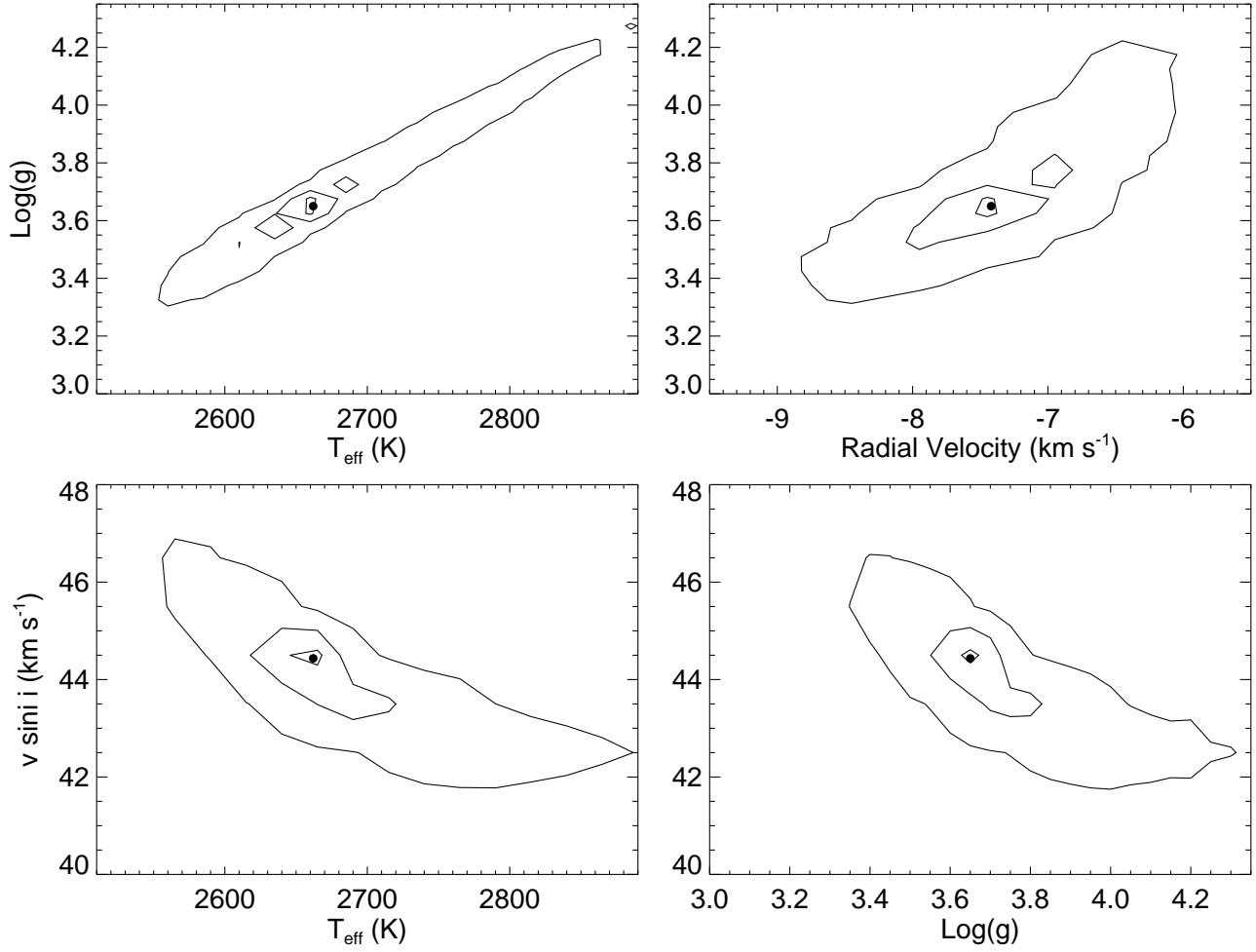


FIG. 2.— The distribution of best-fit values found by the MPFIT procedure with varied input parameters (see §3.3) for the order 65 spectrum ($1.165 - 1.182 \mu\text{m}$) of DENIS 1619–24. Contours mark 10%, 50%, and 90% of the maximum number of points in 25 K, 0.05 dex, 0.5 km s^{-1} (RV) and 0.5 km s^{-1} ($v \sin i$) bins. Filled circles mark our adopted best-fit values. Top left: Effective temperature and surface gravity show a strong degeneracy in this wavelength range. Top right: Radial velocity is well-determined independent of the other parameters. Bottom: Projected rotational velocity is slightly degenerate with both effective temperature and surface gravity. These plots do not show the χ^2 value for each fit result, which is taken into account to determine our adopted best-fit parameters.

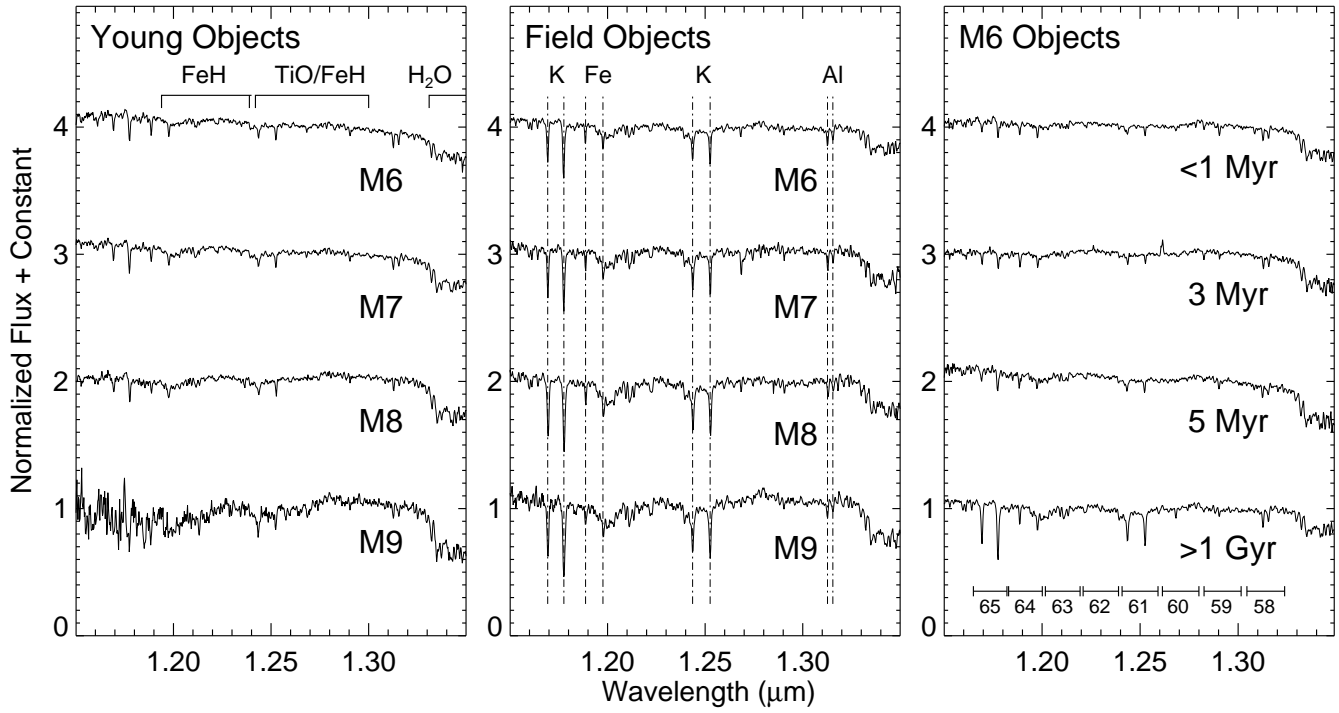


FIG. 3.— Observed J -band spectra of young (age ~ 5 – 10 Myr) M dwarfs (left), field (age ≥ 1 Gyr) M dwarfs (middle), and M6 objects with a range of ages (right). Spectra are normalized at $1.26 \mu\text{m}$ and offset by a constant. The left plot labels molecular absorption bands, the middle plot strong atomic lines, and the right plot the wavelength coverage of NIRSPEC dispersion orders.

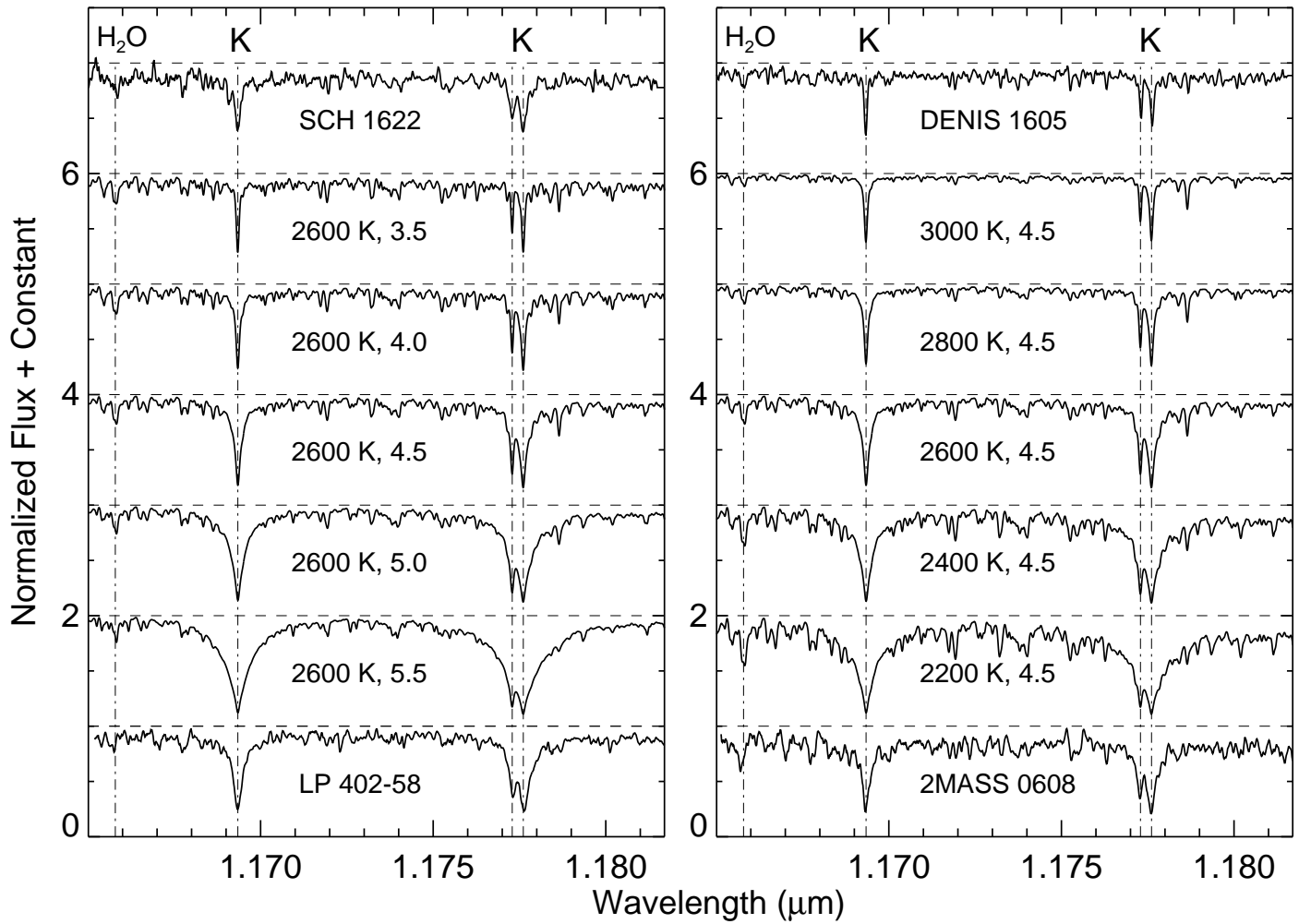


FIG. 4.— High-resolution ($R \sim 20,000$) observed and synthetic spectra for NIRSPEC dispersion order 65. In both panels at top and bottom are observed spectra (SCH 1622–19: M8, 5 Myr; LP 412–31: M8, >1 Gyr; DENIS 1605–24: M6, 5 Myr; 2MASS 0608–27: M8.5, <100 Myr) whereas the five middle spectra are synthetic spectra with effective temperature and log surface gravity as labeled. Horizontal lines denote vertical offsets in the pseudo-continuum levels. The strongest absorption lines are marked by dot-dashed lines and labeled on the plot. The effects of increasing surface gravity (left) and decreasing temperature (right) on the pressure-sensitive K I lines are similar but can be disentangled at high resolution, e.g. using the strength of the H₂O line at 1.16579 μm and other molecular lines.

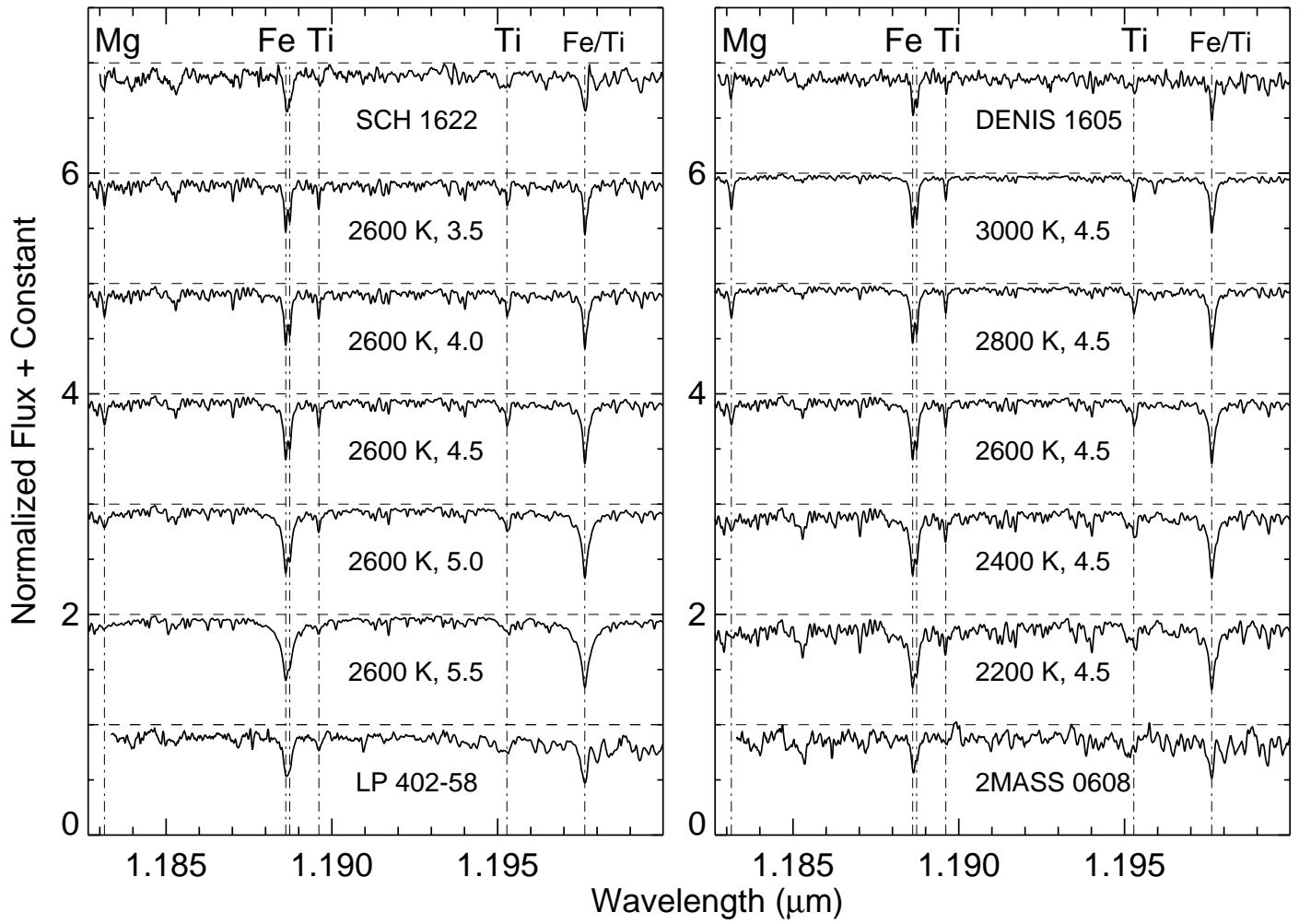


FIG. 5.— The same as Figure 4 but for NIRSPEC dispersion order 64.

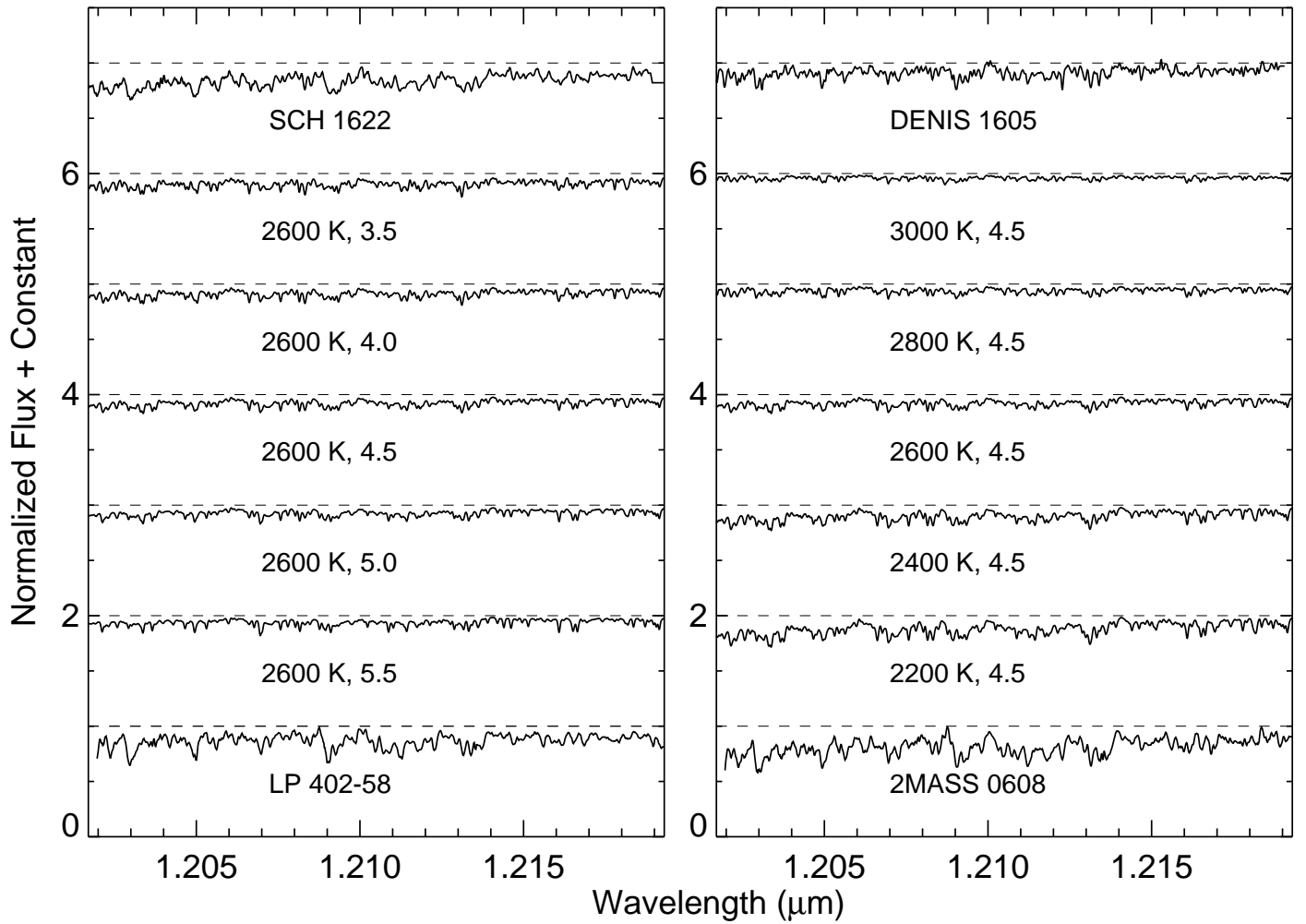


FIG. 6.— The same as Figure 4 but for NIRSPEC dispersion order 63. The spectral features in this order are primarily H_2O and FeH , the latter of which is too weak in the atmosphere models (see § 5.2).

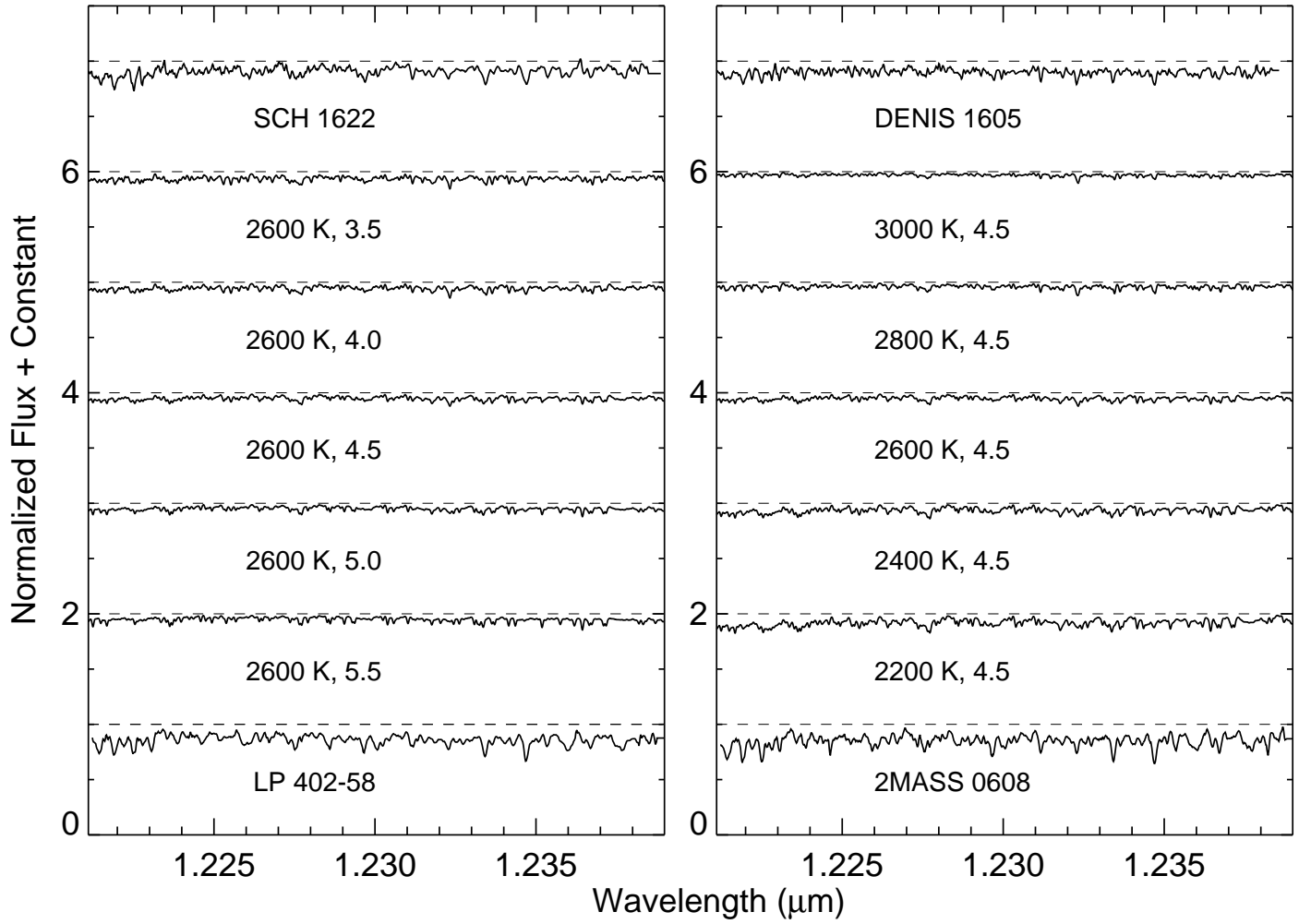


FIG. 7.— The same as Figure 4 but for NIRSPEC dispersion order 62. The spectral features in this order are primarily H_2O and FeH , and again FeH is too weak in the atmosphere models (see § 5.2), notably the the Q -branch of the $F^4\Delta_{7/2}-X^4\Delta_{7/2}$ system from 1.221 to 1.223 μm .

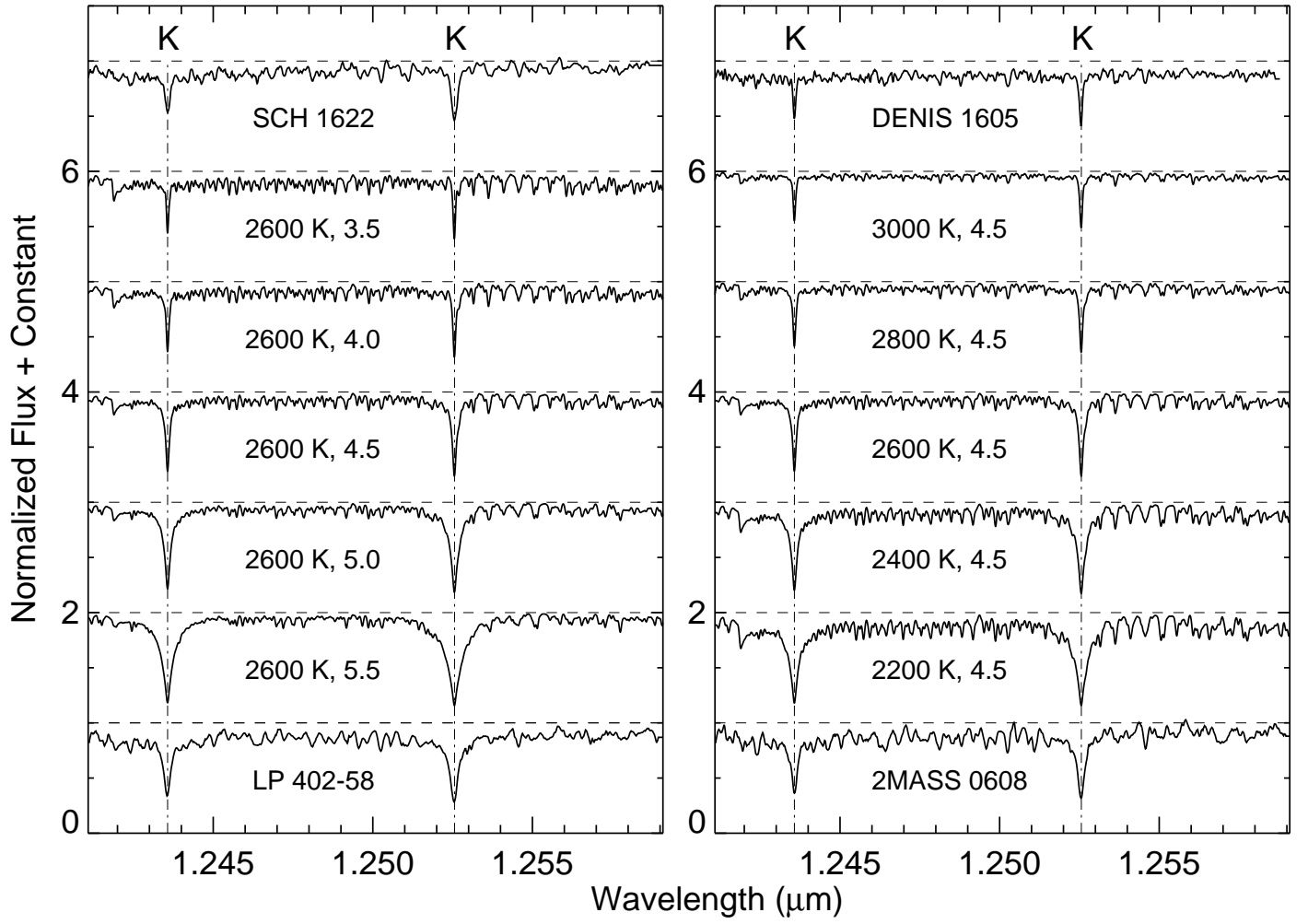


FIG. 8.— The same as Figure 4 but for NIRSPEC dispersion order 61. Regularly-spaced lines in the synthetic spectra are from TiO. In the observed spectra TiO (if present) is blended with FeH, but FeH is considerably weaker in the atmosphere models (see § 5.2).

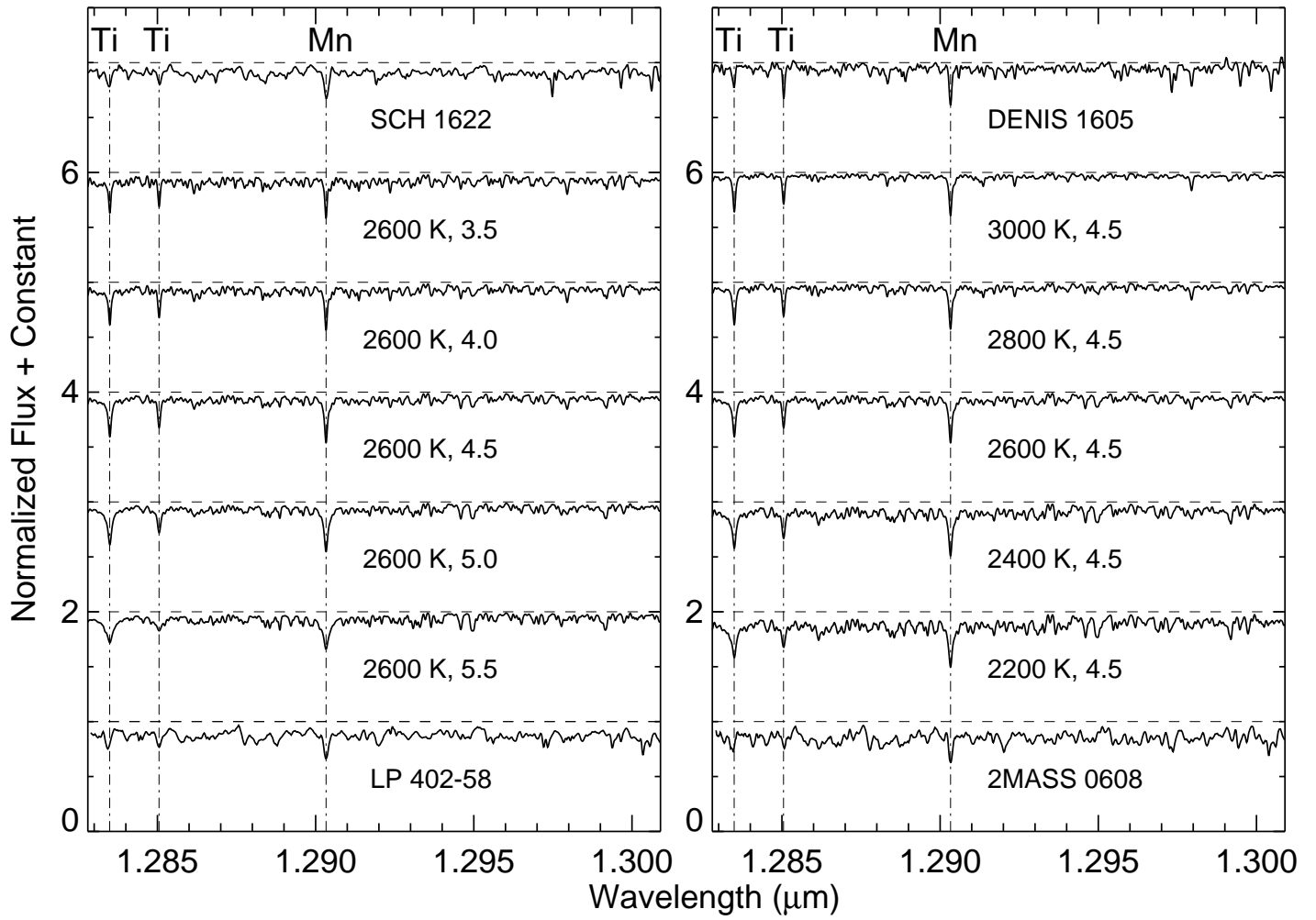


FIG. 9.— The same as Figure 4 but for NIRSPEC dispersion order 59.

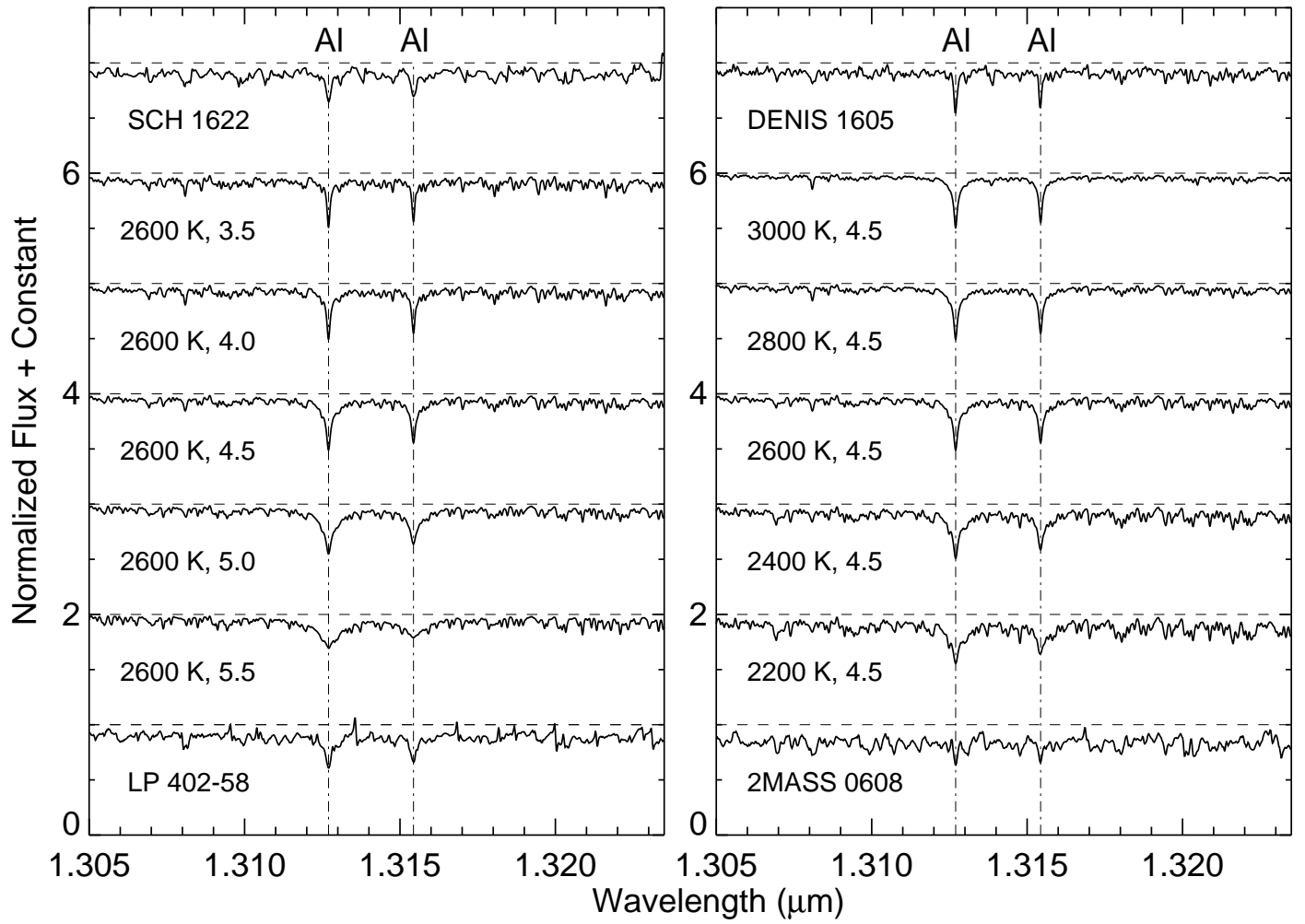


FIG. 10.— The same as Figure 4 but for NIRSPEC dispersion order 58.

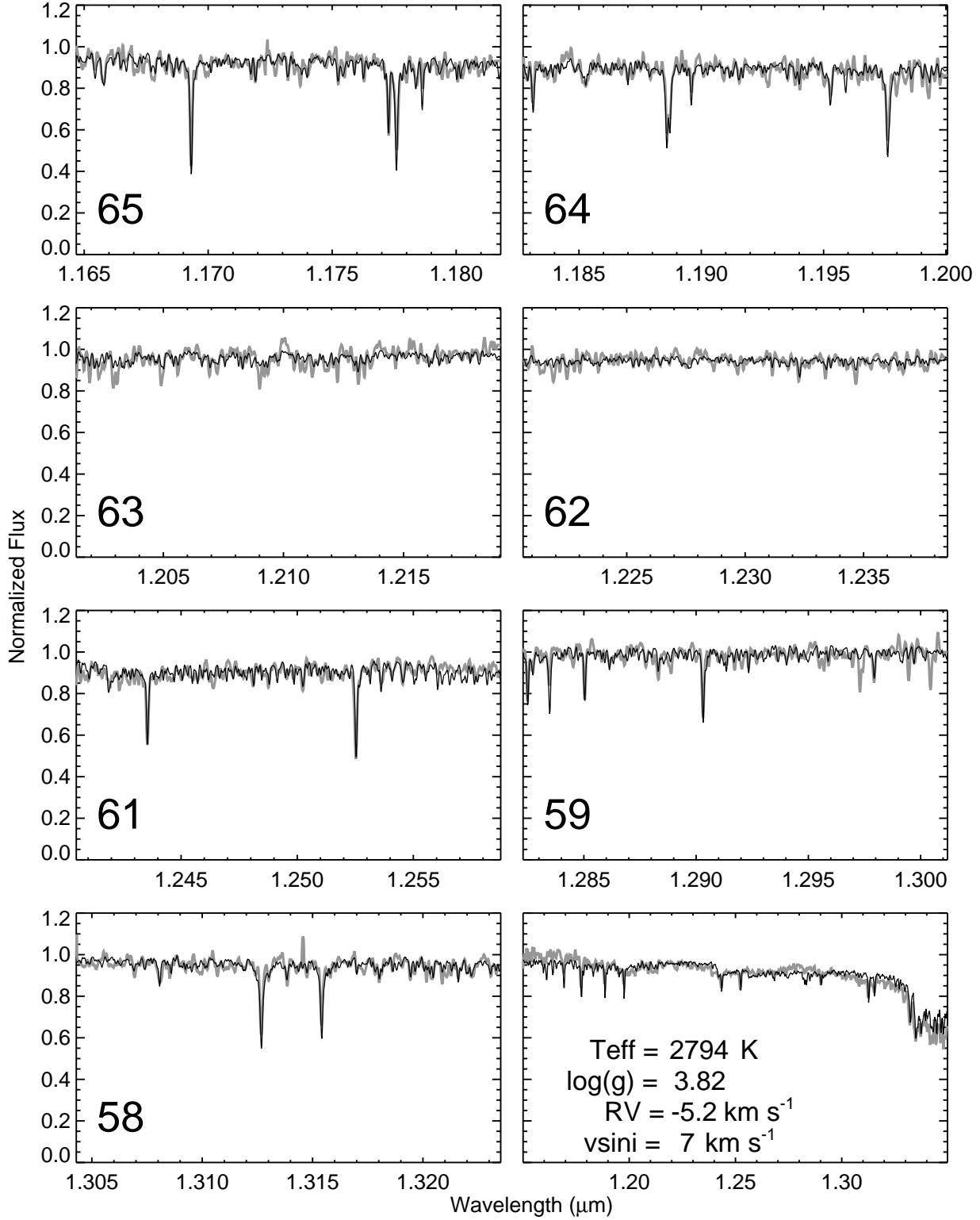


FIG. 11.— Observed (gray) and best-fit synthetic spectra (black) for the young (5 Myr) M6 object DENIS 1605–24. The NIRSPEC dispersion orders are labeled, and the best-fit atmosphere model parameters are given in the bottom-right panel, which is the medium-resolution spectrum across the entire *J* band.

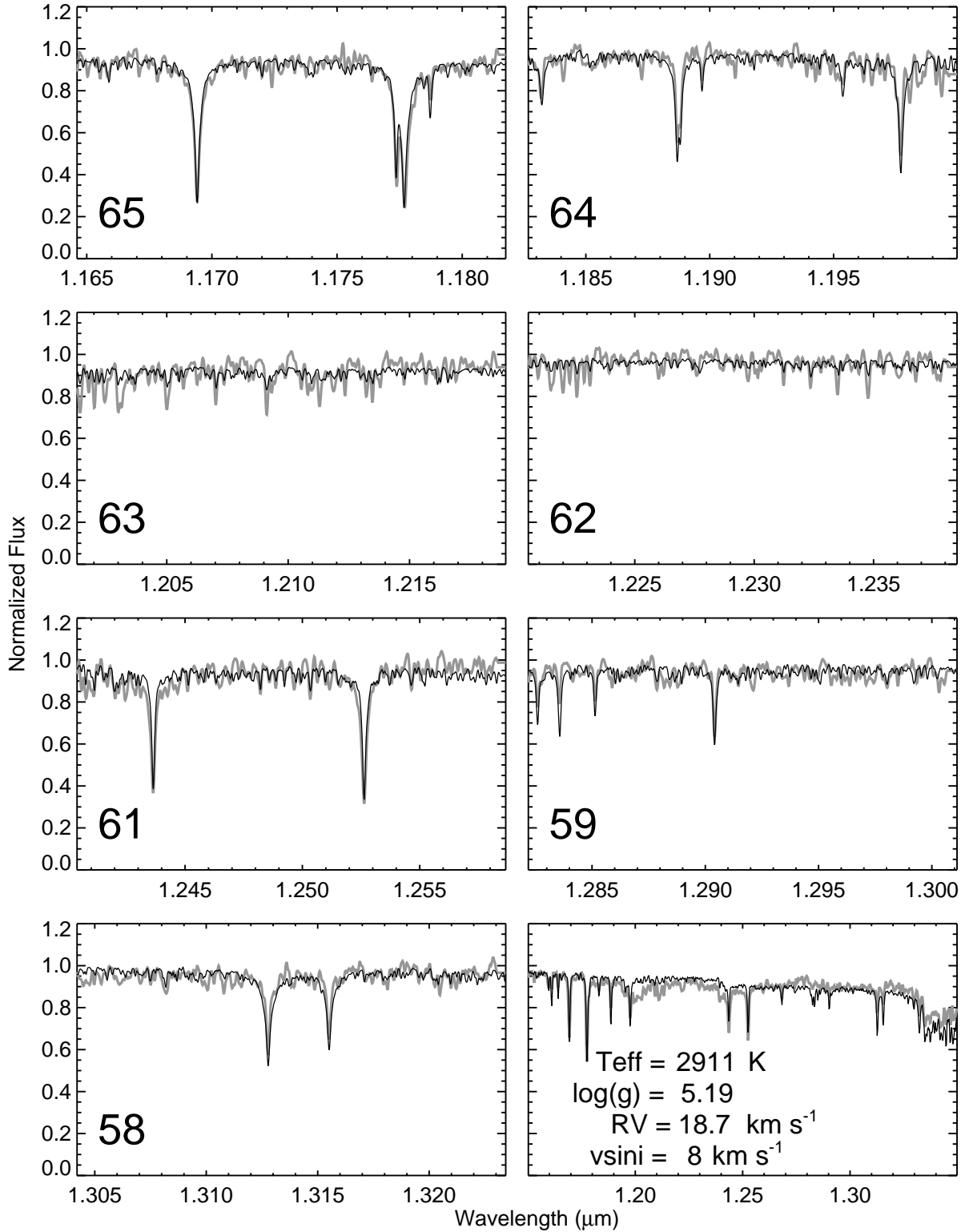


FIG. 12.— Observed (gray) and best-fit synthetic spectra (black) for the field (old, >1 Gyr) M6 dwarf Gl 406. The NIRSPEC dispersion orders are labeled, and the best-fit atmosphere model parameters are given in the bottom-right panel. Note the poor fit for the observed FeH features at both high- and medium-resolutions (see § 5.2).

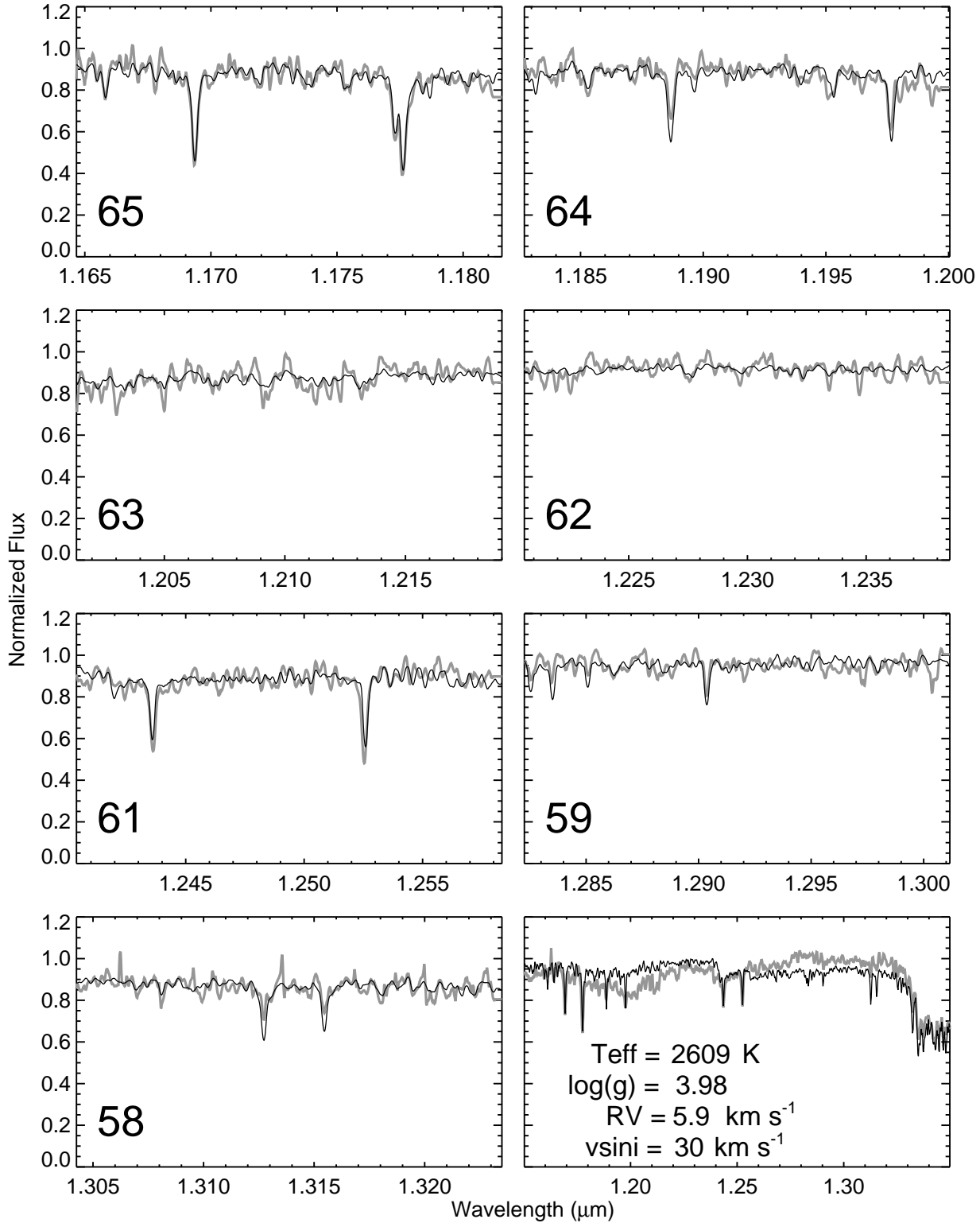


FIG. 13.— Observed (gray) and best-fit synthetic spectra for the young (~ 10 Myr) M8 TW Hydrae member 2MASS 1139–31. The NIRSPEC dispersion orders are labeled, and the best-fit atmosphere model parameters are given in the bottom-right panel. Again, note the poor fit to FeH features (see § 5.2).

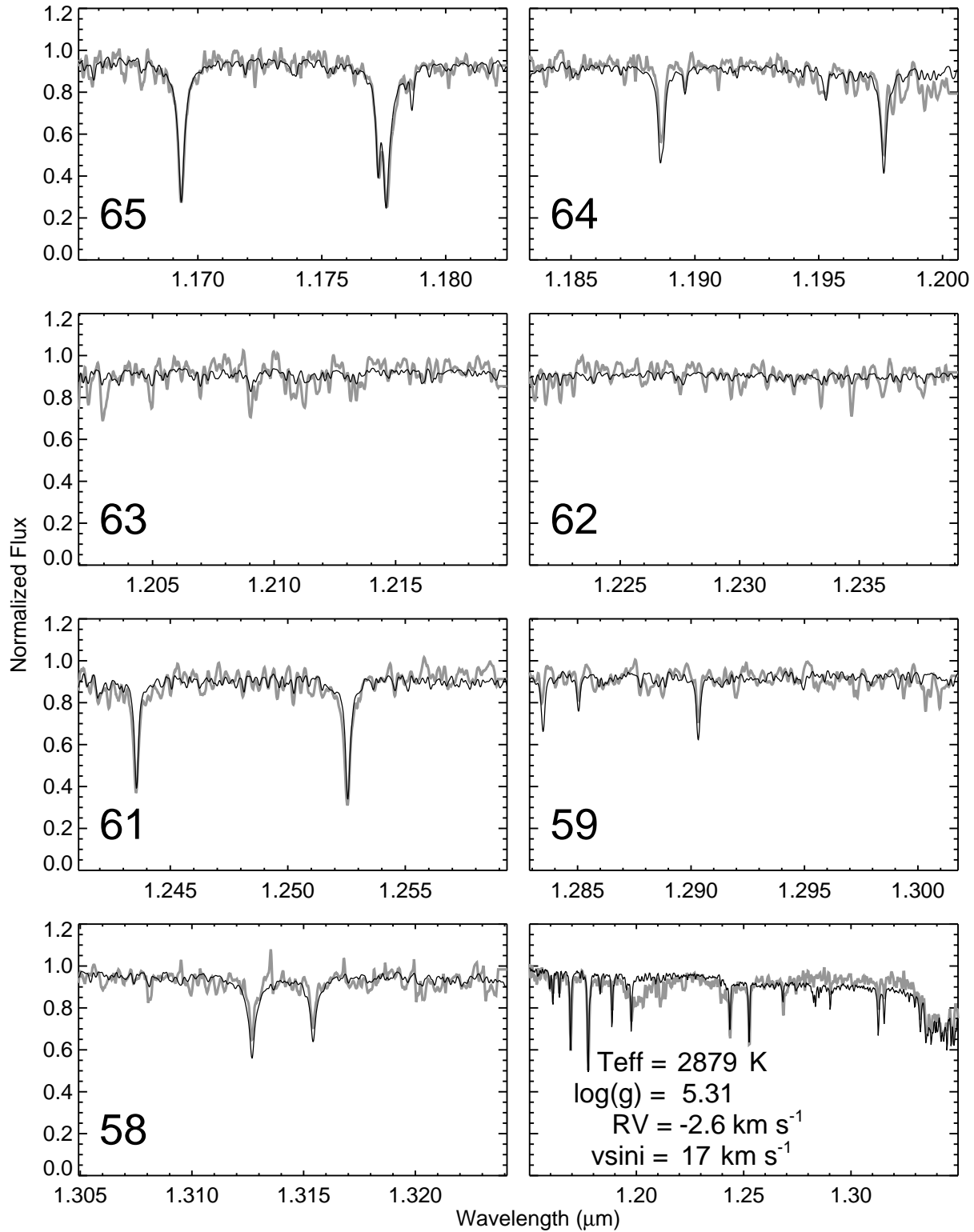


FIG. 14.— Observed (gray) and best-fit synthetic spectra for the field (old, >1 Gyr) M7 dwarf LP 402-58. The NIRSPEC dispersion orders are labeled, and the best-fit atmosphere model parameters are given in the bottom-right panel.

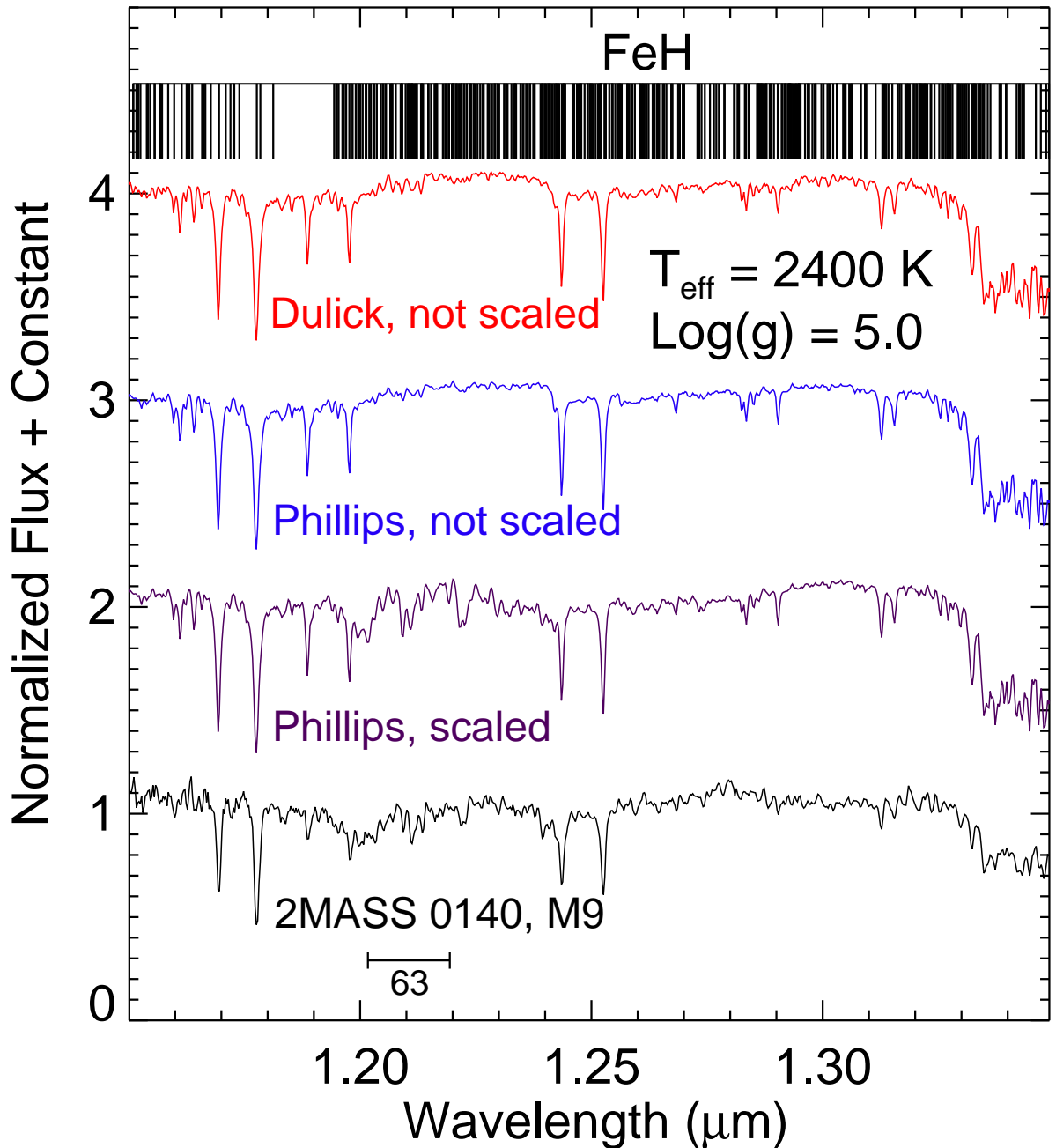


FIG. 15.— Synthetic spectra produced using the same atmospheric structure ($T_{\text{eff}}=2400$ K and $\log(g)=5.0$) but different FeH line lists and oscillator-strength scalings as indicated on the plot. The NIRSPEC medium-resolution spectrum of the M9 dwarf 2MASS 0140+17 is plotted for comparison, and the horizontal bar marks the wavelength range of NIRSPEC order 63 shown in Figure 16. While the difference between the Dulick et al. (2003) and the unscaled Phillips et al. (1987) line lists are imperceptible at this resolution, the scaled Phillips et al. (1987) oscillator strengths make a dramatic difference in the spectra from 1.205 to 1.240 μm , resulting in a much better match to the observed data. See § 5.2 for a detailed discussion.

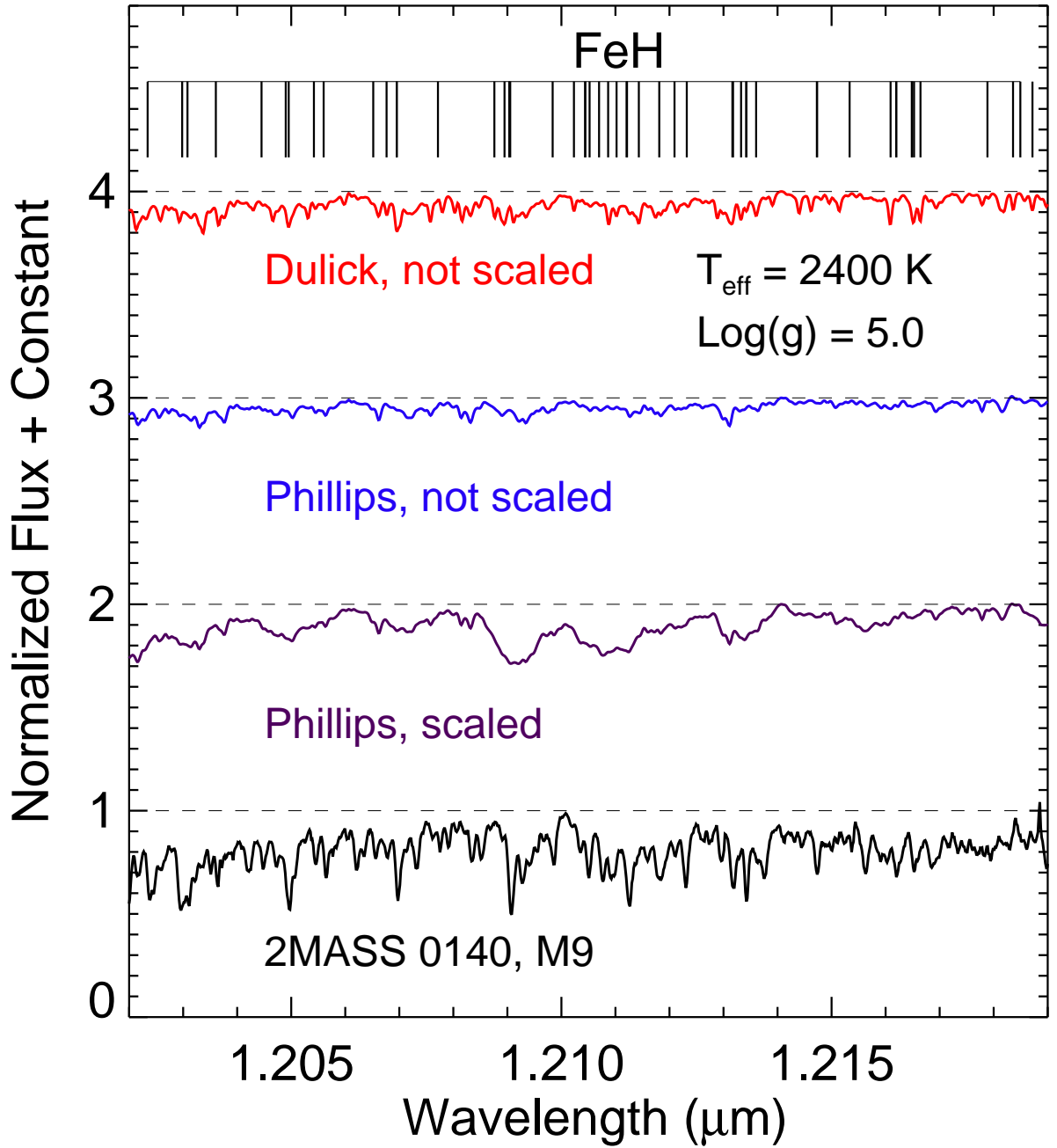


FIG. 16.— Synthetic spectra produced using the same atmospheric structure ($T_{\text{eff}}=2400 \text{ K}$ and $\log(g)=5.0$) but different FeH line lists and oscillator-strength scalings as indicated on the plot. NIRSPEC dispersion order 63 spectrum of the M9 dwarf 2MASS 0140+27 is plotted for comparison. The synthetic spectrum using the Dulick et al. (2003) line list shows an improved correspondence over the Phillips et al. (1987) line list for individual features in the 2MASS 0140+27 spectrum, but the line strengths are too weak in the atmosphere model. See § 5.2 for a detailed discussion.

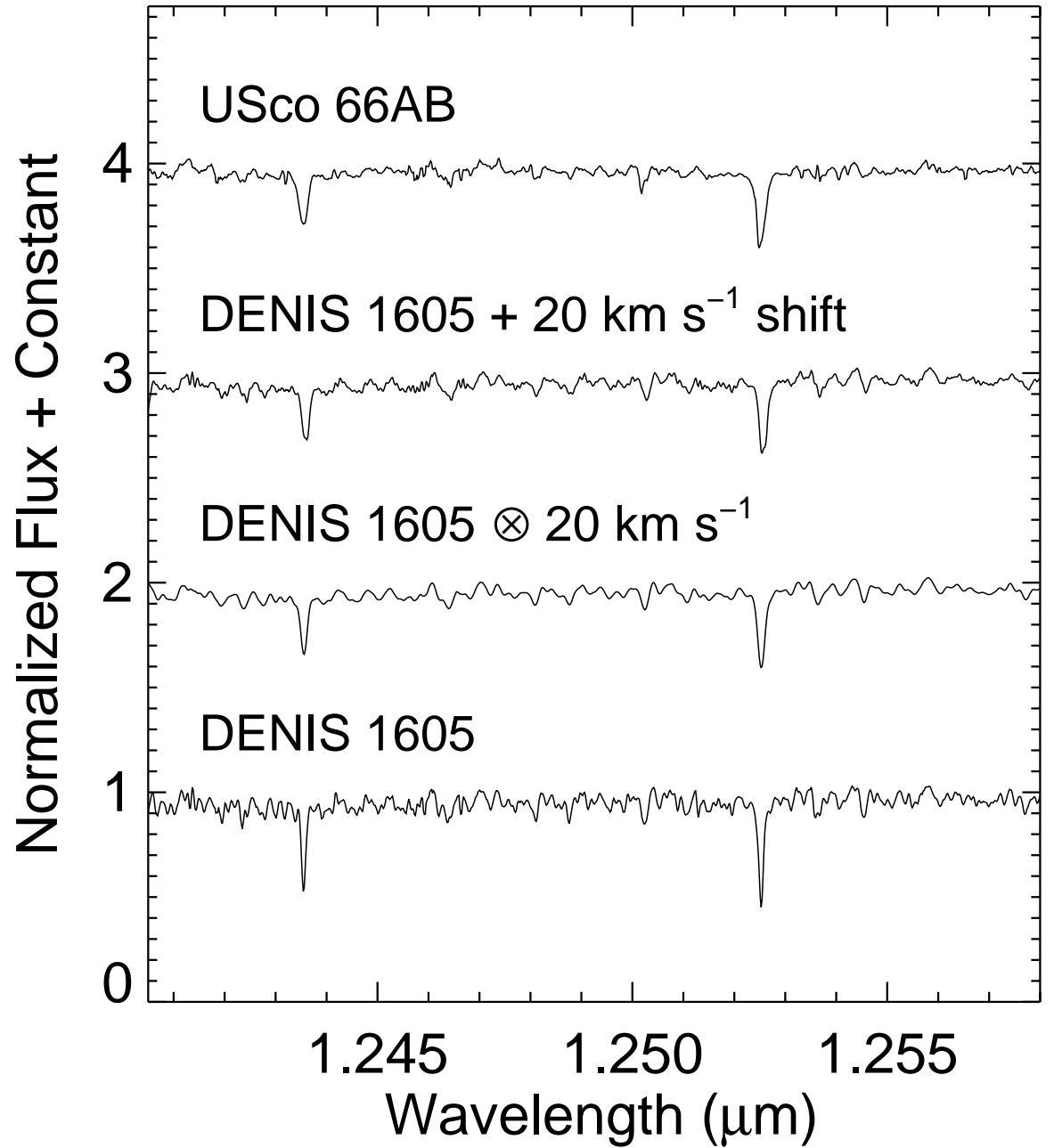


FIG. 17.— Observed NIRSPEC dispersion order 61 spectra of USco 66AB (top) and DENIS 1605–24 (bottom). The second-to-top spectrum are formed by shifting the spectrum of DENIS 1605–24 ($\log(g)=3.82$, $v\sin i \leq 7 \text{ km s}^{-1}$) by 20 km s^{-1} , the result added to the unshifted spectrum, and renormalizing. The second-from-bottom spectrum is the spectrum of DENIS 1605–24 convolved with a rotational velocity profile of 20 km s^{-1} . Both the shifted and convolved spectra resemble the spectrum of USco 66AB ($\log(g)=4.26$, $v\sin i=28 \text{ km s}^{-1}$), indicating that binarity may influence the inferred $v\sin i$ and/or $\log(g)$. This is unlikely to be the case for USco 66AB, for which the *known* binary would induce no more than a few km s^{-1} shift in the spectrum (assuming a circular orbit), but could be a factor in as yet unresolved objects such as DENIS 1619–24 and SCH 1622–19.

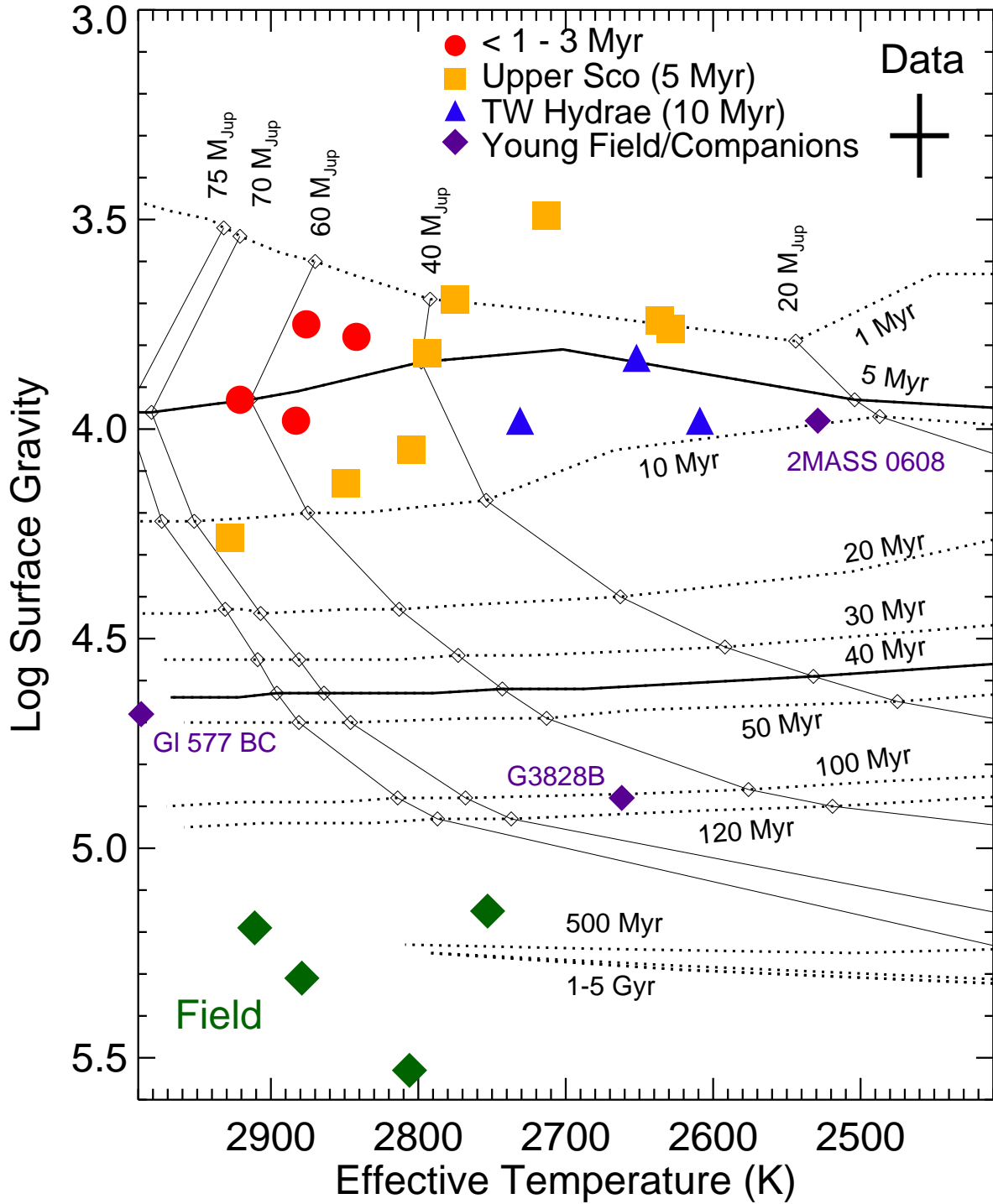


FIG. 18.— Adopted physical properties of young objects ($\log(g) < 4.3$) plotted with the DUSTY00 tracks from Chabrier et al. (2000); Baraffe et al. (2002). Membership (and/or approximate age) are indicated by different symbols: circles for ρ Ophiuchi, Taurus, LHA233 group, and σ Orionis objects; squares for Upper Scorpius objects; triangles for TW Hydrae objects, and diamonds for candidate young field objects and companions. The error bars in the upper right represent typical uncertainties based on Monte Carlo simulations (see § 3.3); systematic uncertainties in the atmosphere models are likely larger.

TABLE 1
Observing Log

Object Name ^a	Spec. Type	R.A. (J2000.0)	Dec. (J2000.0)	J^b (mag)	Int. Time (seconds)	UT Date of Observation ^c	Ref.
Gl 577BC	M5.5	15 05 49.9	+64 02 50	7.19	1200	2006 May 19	1
					600	2003 Mar 24	3
Gl 406 (Wolf 359)	M6	10 56 28.9	+07 00 53	7.09	240	2006 May 20	1
					120	2000 Dec 6	2
CFHT Tau-7	M5.75	04 32 17.2	+24 22 11	11.52	1200	2008 Mar 19	1
					600	2009 Nov 08	1
σ Orionis 12	M6	05 37 57.5	−02 38 44	14.23	6000	2008 Dec 06	1
					1200	2003 Dec 4	3
UScoCTIO 66AB	M6	16 01 49.6	−23 51 08	12.91	2400	2007 May 29	1
					600	2003 May 12	3
DENIS-P J160514.0-240652	M6	16 05 14.0	−24 06 52	12.84	2400	2007 May 29	1
					1200	2004 May 2	3
GY 5 (ISO-Oph 30)	M6	16 26 21.5	−24 26 01	12.57	2400	2007 May 31	1
					600	2003 May 14	3
2MASS J22344161+4041387AB	M6	22 34 41.6	+40 41 39	12.57	2400	2007 May 29	1
					600	2003 Dec 4	3
SCH J16121188-20472698	M6.5	16 12 11.9	−20 47 27	13.66	4800	2007 May 29	1
					1200	2009 Apr 7	1
LP 402-58	M7	23 36 43.9	+21 53 39	12.71	3600	2008 Dec 7	1
					600	2004 Nov 6	3
UScoCTIO 100	M7	16 02 04.3	−20 50 43	12.84	2400	2007 May 30	1
					600	2003 May 13	3
UScoCTIO 130	M7.5	15 59 43.7	−20 14 40	14.20	4800	2007 May 30	1
					1200	2004 Apr 30	3
LP 412-31	M8	03 20 59.7	+18 54 23	11.74	2400	2008 Dec 7	1
					600	2000 Dec 4	2
SCH J16235158-23172740	M8	16 23 51.7	−23 17 26	13.55	3600	2008 Mar 20	1
					600	2009 Apr 7	1
DENIS-P J161929.9-244047	M8	16 19 29.9	−24 40 47	14.23	2400	2007 May 30	1
					1200	2004 Jul 22	3
SCH J16224384-19510575	M8	16 22 43.8	−19 51 06	12.35	2400	2008 Mar 19	1
					600	2009 Apr 7	1
2MASS J11395113-3159214	M8	11 39 51.1	−31 59 21	12.69	3600	2006 May 19	1
					1200	2001 Dec 30	3
2MASS J12073347-3932540AB	M8	12 07 33.4	−39 32 54	13.00	2400	2007 May 29	1
					1200	2001 Dec 30	3
2MASS J06085283-2753583	M8.5	06 08 52.8	−27 53 58	13.60	4800	2008 Dec 6	1
					600	2003 Dec 4	3
TWA 5B	M8.5	11 31 55.4	−34 36 29	7.67	1200	2006 May 20	1
					600	2002 Dec 24	3
2MASS J01400263+2701505	M9	01 40 02.6	+27 01 50	12.49	2400	2000 Dec 4	4
					600	2009 Nov 08	1

REFERENCES. — (1) this work, (2) McLean et al. 2003, (3) McGovern 2005, (4) McLean et al. 2007

^a 2MASS, DENIS, and SCH object names are truncated in subsequent tables and in the text.

^b From 2MASS All-Sky Point Source Catalog. The magnitudes for the close companions Gl 577BC and TWA 5B are for the combined system because they are unresolved in 2MASS.

^c The first entry for each object refers to high-resolution (echelle) observations and the second entry, if present, refers to medium-resolution (non-echelle) observations. References for these observations, if previously published, are given in the last column.

TABLE 2
Sample Properties

Object Name	Spec. Type	Notes	Ref.
Upper Scorpius (~ 5 Myr)			
USco 66AB	M6	q ~ 1 binary	1, 2
DENIS 1605–24	M6	...	3
SCH 1612–20	M6.5	...	4
USco 100	M7	...	1
USco 130	M7.5	Estimated spectral type	1
SCH 1623–23	M8	...	4
DENIS 1619–24	M8	Possible spectroscopic binary	3, 4
SCH 1622–19	M8	Possible unresolved binary	5
TW Hydrae (~ 10 Myr)			
2MASS 1139–31	M8	...	6
2MASS 1207–39AB	M8	q ~ 0.3 binary	6, 7
TWA 5B	M8.5	Companion	8
Other Young Objects			
GY 5 (ISO-Oph 30)	M6	ρ Ophiuchi, $\lesssim 1$ Myr	9
2MASS 2234+40AB	M6	Lk H α 233, ~ 1 Myr, q ~ 1 binary	10
CFHT Tau-7	M5.75, M6.5	Taurus, 1.5 Myr	11, 12
σ Ori 12	M6	σ Orionis, ~ 3 Myr	13
Gl 577BC	M5.5	Companion, ~ 70 Myr, q ~ 1 binary	14
2MASS 0608–27	M8.5	Young Field, ≤ 100 Myr	15
Field Objects (≥ 1 Gyr)			
Gl 406 (Wolf 359)	M6	RV standard	16
LP 402-58	M7	...	17
LP 412-31	M8	Strongly flaring object	17, 18
2MASS 0140+27	M9	...	16

REFERENCES. — (1) Ardila et al. (2000), (2) Kraus et al. (2005), (3) Martín et al. (2004), (4) (Mohanty et al. 2005)(5) Slesnick et al. (2006), (6) Gizis (2002), (7) Mohanty et al. (2007), (8) Lowrance et al. (1999), (9) Wilking et al. (1999), (10) Allers et al. (2009), (11) Luhman (2006), (12) Guieu et al. (2006), (13) Béjar et al. (1999), (14) Lowrance et al. (2005), (15) Kirkpatrick (2008), (16) McLean et al. (2007), (17) Gizis et al. (2000), (18) Schmidt et al. (2007).

TABLE 3
Spectral Fitting Results - Effective Temperatures

Object	Spec. Type	Prev. T_{eff}^a	N3	65	64	63	62	61	59	58	Adopted T_{eff}
USco 66AB	M6	2851–3000	2973	2927	2939	(2800)	2250	2988	(3000)	(2881)	2928
DENIS 1605–24	M6	2850–3000	2826	2785	2739	(2537)	(2800)	(2977)	2921	2800	2794
SCH 1612–20	M6.5	2630–2935	2840	2804	2757	2531	2699	(3000)	2999	2624	2777
USco 100	M7	2672–2880	2880	2825	2813	-(2651)-	-(2998)-	(2912)	(3000)	(2746)	2849
USco 130	M7.5	2550–2850	2660	2653	2764	(2800)	(2883)	(2826)	(2978)	(2741)	2805
SCH 1623–23	M8	2455–2710	2625	(2489)	(2780)	(2351)	-(2458)-	(2741)	-(2899)-	-(2664)-	2636
DENIS 1619–24	M8	2600–2710	2726	(2666)	(2770)	2645	2906	(2776)	(2810)	(2558)	2713
SCH 1622–19	M8	2400–2710	2594	2594	(2632)	(2261)	(2376)	(2800)	-(2939)-	-(2792)-	2629
2MASS 1139–31	M8	2400–2710	(2435)	2486	(2701)	(2409)	-(2900)-	(2600)	-(2837)-	(2484)	2609
2MASS 1207–39AB	M8	2400–2710	2485	2602	2694	2405	(2800)	(2801)	(2804)	2486	2652
2MASS 0608–27	M8.5	2150–2555	2200	(2574)	-(2585)-	(2167)	2276	-(2900)-	-(2727)-	-(2474)-	2529
TWA 5B	M8.5	2300–2550	2360	(2716)	(2686)	(2391)	2787	2620	(2904)	(2814)	2731
Gl 406	M6	2670–3058	3000	(3000)	(2833)	2215	(2895)	(2900)	3000	3000	2911
LP 402-58	M7	2600–2620	2864	(2950)	-(2800)-	(2900)	(2799)	(2900)	3000	2960	2879
LP 412-31	M8	2480–2638	2919	(2936)	(2950)	-(2273)-	-(2805)-	(2860)	2800	2600	2806
2MASS 0140+27	M9	2325–2400	2824	(2805)	(2850)	-(2215)-	-(2846)-	-(2900)-	3000	2714	2753

NOTE. — See § 3.3 for explanation of annotations of the table entries.

^a Effective temperature (or range of temperatures) determined by previous studies for the specific object or for an object of the same spectral type and similar age are from Basri et al. (2000); Dahn et al. (2002); Luhman et al. (2003); Gorlova et al. (2003); Mohanty & Basri (2003); Golimowski et al. (2004); Mohanty et al. (2004a); Vrba et al. (2004); McGovern (2005); Reiners & Basri (2007); Slesnick et al. (2006); Scholz et al. (2007); Slesnick et al. (2008); Teixeira et al. (2008); Wilking et al. (1999).

TABLE 4
Spectral Fitting Results - Surface Gravities

Object	Age ^a	Prev. Log(g) ^b	N3	65	64	63	62	61	59	58	Adopted log(g)
USco 66AB	5 Myr	3.64–4.50	4.21	4.32	4.20	(4.69)	5.40	4.72	(3.80)	(3.92)	4.26
DENIS 1605–24	5 Myr	4.25	3.70	3.60	3.49	(3.60)	(4.47)	(4.67)	3.94	3.14	3.82
SCH 1612–20	5 Myr	3.57–3.61	3.50	3.66	3.46	3.81	3.53	(4.67)	3.80	3.01	3.68
USco 100	5 Myr	3.55–4.50	4.10	4.09	3.82	–(4.70)–	–(5.69)–	(4.75)	(3.72)	(3.09)	4.13
USco 130	5 Myr	3.25–4.00	3.82	3.92	3.56	(4.70)	(4.35)	(4.67)	(3.99)	(3.12)	4.05
SCH 1623–23	5 Myr	3.27–3.32	3.66	(3.57)	(3.48)	(3.89)	–(4.41)–	(4.46)	–(3.61)–	–(3.00)–	3.74
DENIS 1619–24	5 Myr	4.00	3.52	(3.66)	(3.38)	5.27	5.76	(4.19)	(3.21)	(3.00)	3.49
SCH 1622–19	5 Myr	3.02–3.06	3.70	3.89	(3.38)	(3.79)	(3.56)	(4.77)	–(3.85)–	–(3.01)–	3.76
2MASS 1139–31	10 Myr	3.62–4.25	(3.30)	3.76	(3.82)	(4.03)	–(5.59)–	(4.30)	–(3.57)–	(3.33)	3.98
2MASS 1207–39AB	10 Myr	4.00–4.25	3.30	3.90	3.50	3.66	(4.60)	(4.65)	(3.40)	3.00	3.83
2MASS 0608–27	<100 Myr	4.00	3.20	(4.42)	–(3.61)–	(3.92)	3.60	–(5.57)–	–(3.40)–	–(3.00)–	3.98
TWA 5B	10 Myr	3.75–3.98	3.10	(4.12)	(3.50)	(4.20)	4.34	5.26	(3.60)	(3.53)	3.88
Gl 406	>1 Gyr	5.15–5.40	5.67	(5.61)	(4.56)	3.62	(4.85)	(5.60)	4.15	4.31	5.19
LP 402-58	>1 Gyr	5.15–5.40	5.35	(5.55)	–(4.70)–	(5.60)	(4.56)	(5.73)	4.00	3.99	5.31
LP 412-31	>1 Gyr	5.15–5.40	6.00	(6.00)	(6.00)	–(3.88)–	–(4.79)–	(6.00)	3.60	4.20	5.53
2MASS 0140+27	>1 Gyr	5.15–5.40	5.83	(5.51)	(5.10)	–(3.61)–	–(4.88)–	–(6.00)–	3.71	3.40	5.15

NOTE. — See § 3.3 for explanation of annotations of the table entries.

^a Age references: Gizis et al. 2000; Preibisch et al. 2002; Zuckerman & Song 2004; Barrado y Navascués 2006; Kirkpatrick 2008

^b Surface gravities determined by previous studies for young objects are from Gorlova et al. (2003); Mohanty et al. (2004a); McGovern (2005); Barrado y Navascués (2006); Slesnick et al. (2006, 2008); Teixeira et al. (2008). The range of surface gravity for field objects (age >1 Gyr) is set by evolutionary models of Chabrier et al. (2000) and Baraffe et al. (2002).

TABLE 5
M6 Sequence - Effective Temperatures

Object	Spec. Type	Prev. ^a T _{eff} ^a	N3	65	64	63	62	61	59	58	Adopted T _{eff}
GY 5	M6 ^b	2700–3050	2871	2939	2814	(2676)	(2788)	(3000)	(3000)	2845	2876
2MASS 2234+40AB	M6	2990	2938	2950	2929	(3000)	(3000)	3000	2913	2617	2921
CFHT Tau-7	M6 ^c	2935–3024	2740	2805	2801	(2701)	(2775)	2946	2969	2760	2825
σOri 12	M6	2990	2779	2973	2833	2650	2700	3000	2939	2793	2842
DENIS 1605–24	M6	2850–3000	2826	2985	2739	(2537)	(2800)	(2977)	2921	2800	2794
Gl 577BC	M5.5	2900–292	3000	3000	(2961)	–(3000)–	(2970)	(2999)	(3000)	(3000)	2988
Gl 406	M6	2670–3058	3000	(3000)	(2833)	2315	(2895)	(2900)	3000	3000	2911

NOTE. — See § 3.3 for explanation of annotations of the table entries.

^a Effective temperature (or range of temperatures) determined by previous studies for the specific object or for an object of the same spectral type and similar age are from Luhman & Rieke (1999); Luhman et al. (2003); Lowrance et al. (2005); Mohanty et al. (2005); Wilking et al. (2005); Gatti et al. (2006); Guieu et al. (2006).

^b Classified as M5.5 by Wilking et al. (2005)

^c Classified as M5.75 by Luhman (2006) and as M6.5 by Guieu et al. (2006)

TABLE 6
M6 Sequence - Surface Gravities

Object	Age	Prev. Log(g)	N3	65	64	63	62	61	59	58	Adopted Log(g)
GY 5	≤1 Myr	3.65	3.80	3.57	3.30	(4.14)	(4.08)	(4.39)	(3.80)	3.24	3.75
2MASS 2234+40AB	~1 Myr	4.00	3.80	3.54	3.56	(5.00)	(4.81)	4.19	3.69	3.60	3.93
CFHT Tau-7	1.5 Myr	...	3.50	3.40	3.44	(4.00)	(4.16)	4.32	3.80	3.10	3.72
σOri 12	3 Myr	4.00	3.70	4.05	3.59	3.61	3.74	4.49	3.78	3.21	3.78
DENIS 1605–24	5 Myr	4.25	3.70	3.60	3.49	(3.60)	4.47	4.67	3.94	3.14	3.82
Gl 577BC	70 Myr	4.75	4.43	4.87	(4.56)	–(5.59)–	(4.87)	(5.09)	(3.80)	(4.07)	4.68
Gl 406	>1 Gyr	5.15–5.40	5.67	(5.61)	(4.56)	3.62	(4.85)	5.60	4.15	4.31	5.19

REFERENCES. — Age and gravity from Luhman & Rieke (1999); Lowrance et al. (2005); McGovern (2005); Mohanty et al. (2005); Wilking et al. (2005); Caballero (2007); Allers et al. (2009).

NOTE. — See § 3.3 for explanation of annotations of the table entries.

TABLE 7
Velocity Results

Object	Spectral Type	Previous RV (km s ⁻¹)	Results $v \sin i$ (km s ⁻¹)	Current RV (km s ⁻¹)	Results $v \sin i$ (km s ⁻¹)
Upper Scorpius					
USco 66AB	M6	-7.81, -4.4	25.9, 27.5	-5.8	28
DENIS 1605-24	M6	-5.2	≤7
SCH 1612-20	M6.5	-6.8	≤9
USco 100	M7	-7.2, -8.9	43.7, 50	-8.3	50
USco 130	M7.5	-3.91	14, 15.2	-7.1	18
SCH 1623-23	M8	-6.0	53
DENIS 1619-24	M8	-7.0	47
SCH 1622-19	M8	-10.2	25
TW Hydrae					
2MASS 1139-31	M8	11.6, 9.7	25	5.9	30
2MASS 1207-39AB	M8	11.2, 8.7	13	7.5	18
TWA 5B	M8.5	13.4	16	9.7	27
Other Young Objects					
2MASS 2234+40AB	M6	-10.6	...	-13.1	17
CFHT Tau-7	M6.5	15.6	20
σ Ori 12	M6	29.8, 37	...	31.2	18
GY 5	M6	-6.39, -6.3	16.5, 16.8	-7.1	20
GI 577BC	M5.5	-6.2	43
2MASS 0608-27	M8.5	22.6	20
Field Objects					
GI 406	M6	19.1	≤2.9	18.7	≤8
LP 402-58	M7	-2.6	17
LP 412-31	M8	41.6, 44.7	8.9	41.8	33
2MASS 0140+27	M9	9.6, 8.2	6.5	8.6	11

REFERENCES. — Tinney & Reid (1998); Reid et al. (2002); Reid (2003); Mohanty et al. (2003); Mohanty & Basri (2003); Muzerolle et al. (2003); Kenyon et al. (2005); Mohanty et al. (2005); Kurosawa et al. (2006); Reiners & Basri (2007); Allers et al. (2009).